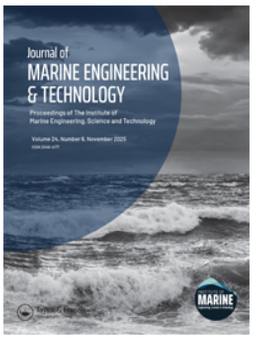

Taylor & Francis
Taylor & Francis Group

Journal of Marine Engineering & Technology

ISSN: 2046-4177 (Print) 2056-8487 (Online) Journal homepage: www.tandfonline.com/journals/tmar20

High-fidelity mean value first principle modelling of dynamic response in spark-ignited marine engines: a comparative analysis of gas path and turbocharger representations

Jasper Vollbrandt, Andrea Coraddu, Rinze Geertsma & Douwe Stapersma

To cite this article: Jasper Vollbrandt, Andrea Coraddu, Rinze Geertsma & Douwe Stapersma (22 Jan 2026): High-fidelity mean value first principle modelling of dynamic response in spark-ignited marine engines: a comparative analysis of gas path and turbocharger representations, Journal of Marine Engineering & Technology, DOI: 10.1080/20464177.2026.2618326

To link to this article: https://doi.org/10.1080/20464177.2026.2618326

Published online: 22 Jan 2026.

JOURNAL OF MARINE ENGINEERING & TECHNOLOGY
https://doi.org/10.1080/20464177.2026.2618326

Taylor & Francis
Taylor & Francis Group

High-fidelity mean value first principle modelling of dynamic response in spark-ignited marine engines: a comparative analysis of gas path and turbocharger representations

Jasper Vollbrandt [a,b], Andrea Coraddu[a], Rinze Geertsma[b] and Douwe Stapersma[a]

[a]Department of Maritime & Transport Technology, Delft University of Technology, Delft, The Netherlands ; [b]Faculty of Military Sciences, Netherlands Defence Academy, Den Helder, The Netherlands

ABSTRACT

As navies and maritime organisations transition towards low-emission propulsion systems, spark-ignited (SI) gas engines capable of operating on sustainable, low-reactivity fuels are gaining renewed interest. These engines, while offering potential for fossil-free operation, present significant challenges under transient conditions due to complex interactions between throttle control, fuel regulation, and combustion stability. Accurate dynamic modelling is critical to integrate these engines into resilient naval power systems and to support the development of advanced control strategies. This study evaluates several high-fidelity mean value first principle engine modelling (MVFPEM) approaches for simulating the dynamic gas path behaviour of a large, high-speed, SI marine engine under rapid load changes. Models with varying levels of complexity, including simplified and full turbocharger implementations and different gas path volume resolutions, were calibrated using a single measurement campaign and validated against measured transient data. Several methods for turbocharger performance mapping (Stapersma, Casey & Robinson, and Jensen) were evaluated for their applicability in predicting the engine behaviour in dynamic operating scenarios. The results highlight that models incorporating three control volumes and full turbocharger dynamics achieve the highest accuracy, particularly during rapid load increases and recovery phases. Simplified models fail to capture turbocharger inertia and pressure transients, limiting their applicability to investigate naval propulsion or electric power generation plant behaviour under transient load conditions. This work provides guidance on selecting and validating engine models for marine applications and reinforces the role of high-fidelity MVFPEMs in the design and simulation of future naval energy systems.

ARTICLE HISTORY
Received 6 May 2025
Accepted 10 January 2026

KEYWORDS
Modelling and simulation; mean value first principle model; filling & emptying; transient performance; alternative fuels; turbocharger prediction

1. Introduction

Worldwide, maritime companies, including navies, are facing serious technical challenges in their strive to reduce greenhouse gas emissions. Since current fuel-cell and battery technology is limited in energy and power density, a shift towards alternative fuels for most shipping activities is imminent (McKinlay et al. 2021; Hoang et al. 2022; Inal et al. 2022). However, marine diesel engines are unable to ignite and combust the majority of alternative fuels, classified as low reactivity fuels. Dual-fuel engines solve this by injecting a small amount of diesel fuel, facilitating the ignition of a low reactivity main fuel. While this technology is already commercially available, relying on diesel as pilot fuel will impede the industries transition to 100% fossil-free. Meanwhile, spark-ignited engines play a minor role in current marine applications due to their inferior fuel efficiency and reliance on expensive low reactivity fuels. However, their ability to combust pure, sustainable, low-reactivity fuel might increase their importance in the near future. To prevent self-ignition of the fuel (knocking), SI-engines operate on lower compression ratios with a penalty on fuel efficiency compared to diesel and dual fuel engines (Heywood 1988), although various technologies are employed for dual fuel systems (Georgescu et al. 2016). Additionally, the cylinder's air-to-fuel ratio must be kept within the stable combustion limit for the specific low reactivity fuel. The majority of large, industrial-type SI-engines use a throttle valve to restrict the mass flow of air to the cylinder. Throttle valves introduce additional engine losses (throttling losses) in case the valve is partly closed and requires an additional control loop to determine set points for the valve. As a result, determining the dynamic response characteristic of these types of engines is more complex due to the interaction of fuel flow control and throttle valve control and the constraining stable combustion limits.

Engine simulation models play a vital role in investigating the dynamic response characteristics. An analysis of different modelling approaches is given in Section 2. Traditionally, fast and computationally inexpensive mean value first principle engine models (MVFPEMs) have been used to examine the dynamic response characteristics of different control approaches or complex power and propulsion generation systems. With ever increasing computational power of modern computers and capable simulation software packages, a shift in the application of the different modelling approaches can be observed. Model fidelity and complexity have progressively increased in modern system design and control development to enable the exploration of a wider range of outputs and control parameters with improved predictive accuracy. This evolution, however, has led to a departure from the original intent and structure of mean-value first-principles engine models (MVFPEMs). In particular, recent modelling practices increasingly diverge from the foundational principles proposed by Hendricks (1997) for control-oriented MVFPEMs, which emphasise that such models should:

CONTACT Jasper Vollbrandt j.vollbrandt@tudelft.nl Faculty of Mechanical Engineering, Delft University of Technology, Building 34, Mekelweg 2, 2628CD Delft, The Netherlands

(1) be physically intuitive;
(2) be easily modifiable for application-specific needs;
(3) follow a modular architecture;
(4) remain simple and mathematically compact;
(5) minimise the number of fitting parameters.

Several approaches to increase the model fidelity for the dynamic response characteristic of MVFPEMs exist, ranging from the simplified implementation of the turbocharger equation by Geertsma et al. (2017) to approaches including a full turbocharger model and representations of every inlet and exhaust volume element (Schulten and Stapersma 2003; Sui et al. 2022). Especially including a full turbocharger model is recognised as an essential building block in predicting the dynamic response, but this requires the availability of the compressor and turbine performance maps. Researchers conclude that MVEM must be suitable for capturing dynamic response characteristics and can be used to investigate the behaviour of electrical power generation or propulsion systems under different circumstances or to develop a control strategy. In most cases, however, authors omit extensive error-calculations between measured and predicted results or state indexes of performance (Ghelardoni et al. 2013; Coraddu et al. 2022) for their chosen gas exchange approach but base their validation on time-trace plots of simulation results and experimental data, see for example (Rakopoulos et al. 2007; Wurzenberger et al. 2010; Theotokatos 2010; Mestemaker et al. 2020; Bondarenko and Fukuda 2020)

This paper aims to compare different simulation approaches for the gas exchange model of an MVFPEM and provide an extensive error analysis for the steady state performance and the dynamic response, thereby introducing several novelties:

- Evaluating the dynamics of a large high-speed, spark-ignited marine gas engine;
- Proposing a single measurement campaign for the calibration and validation of the model, from which steady state operating points will be used to calibrate the models and the measurements of dynamic response will be used for validation;
- Comparing two different approaches to predict the turbocharger performance data from the measurement campaign and validating these approaches on an actual engine;
- Assessing the performance indexes for the different approaches extensively for all relevant engine parameters for the steady state results and the dynamic response characteristics.

2. Background

Since the rise of affordable and capable computers in the 1970s, simulation models have been developed to investigate internal combustion engines. In these early days, most engine simulation models were developed for control purposes. Stricter emission regulations forced engine manufacturers to spend increasing time and effort on the engine test benches, figuring out optimal control approaches to reduce fuel consumption and emissions for every engine speed and load configuration (Baker and Daby 1977). Early simulation models aimed at reducing the required physical testing by deriving a polynomial fit from a reduced test grid, see for example (Hubbard 1975; Blumberg 1976; Cassidy 1977). These models could predict steady state results for fuel consumption and emissions, enabling the evaluation of different control objectives and related control variables such as valve timing, spark timing, exhaust gas recirculation rates and air-to-fuel ratio. Since these models coupled inputs (speed, torque, A/F) more or less directly to outputs (BSFC, exhaust gas composition), the ability to predict other engine parameters was limited (Powell 1987), and it was not possible to predict dynamic response characteristics.

At the same time, introducing turbocharged diesel engines in trucks and cars required a better understanding of their much slower dynamic response compared to naturally aspirating engines due to the turbocharger dynamics. This sparked the development of the first dynamic simulation models (Powell 1987; Rakopoulos and Giakoumis 2006). Solving the first dynamic models of turbocharged diesel engines required the combination of digital computers with analogue computers to solve the differential equations for the crankshaft and turbocharger shaft dynamics (Ledger and Walmsley 1971; Ledger et al. 1971; Parnell 1970), since the first digital computers were slow in the required continuous integration operation. While these models used fewer and simpler relations than current simulation approaches, they already clearly distinguished between the in-cylinder compression and combustion process and the gas-exchange process, including the turbocharger and its dynamics. This distinction is probably even more relevant in current engine simulation models since varying applications will require varying sophistication and completeness of the involved sub-models (Heywood 1988).

The in-cylinder process plays a central role in governing heat release during combustion, affecting both heat-release and combustion efficiencies, which in turn influence emissions formation. Sub-models for the in-cylinder process thus vary in their complexity, accuracy and computational cost. Simple models may rely on mapped in-cylinder data, similar to the very first input/output models. These models cannot predict engine operation outside the measured grid, but they are very easy to set up and require little computational resources (Powell 1987). Although these models are easy to set up, obtaining sufficient and suitable measurement data for the complete engine envelope can be challenging, often requiring a sophisticated engine test bed. Predicting the dynamic response characteristics with these models is hardly feasible. Based on first principles, mean value models offer more insight and can predict averaged in-cylinder parameters (Rakopoulos and Giakoumis 2009). In such models, the flow of air and exhaust gases through the engine, particularly within the cylinder, is not resolved at every crank angle; instead, it is averaged over the discrete closed in-cylinder process. The heat release of the combusted fuel in mean value models is often described by thermodynamic cycles such as the Otto-cycle for gasoline engines (Angulo-Brown et al. 1994; Eriksson and Andersson 2002; Curto-Risso et al. 2008) and the Diesel or Seiliger cycle for diesel engines (Geertsma et al. 2017; Sui et al. 2017; Sein and Bo 2020; Sui et al. 2022). Simpler mean value models determine the heat release by the amount of injected fuel and a heat release efficiency (Brugård et al. 2001; Chesse et al. 2004). If more detailed results of the combustion process are required, describing the heat release based on a thermodynamic cycle is insufficient and should instead be crank-angle resolved (Baldi et al. 2015; Guan et al. 2015). The heat release of combusted fuel in 0-D models is often described with a Wiebe function (Heywood 1988; Merker et al. 2005), specifying the mass fraction of burned fuel versus the crank-angle. Based on the type of fuel, multiple Wiebe functions can be combined, for example: diesel combustion described with a single Wiebe function (Baldi et al. 2015; Guan et al. 2015; Theotokatos et al. 2018) or a double Wiebe function (Scappin et al. 2012; Maroteaux et al. 2015; Sun et al. 2017; Tadros et al. 2019), the combustion of natural gas described by a double Wiebe function (Sapra et al. 2020), a dual-fuel combustion by a double (Xu et al. 2017) or triple Wiebe function (Caligiuri and Renzi 2017; Stoumpos et al. 2018) or a mixture of ethanol and gasoline with a double Wiebe function (Yeliana et al. 2011).

To predict emissions arising during the combustion of different fuels, a combustion model containing reaction mechanisms and kinetics can be added (Theotokatos et al. 2018). The majority of engine research is interested in the formation of NO_x, but the

formation of CO_x and SO_x and the emission of unburned hydrocarbons (UHC) and particulate matter can also be predicted, depending on the implemented combustion model (Stoumpos et al. 2018). The simplest combustion model consists of one zone, effectively lumping the fuel and combustion products together in one thermodynamic control volume (Sapra et al. 2020; Rakopoulos et al. 2008). These approaches can be used to describe the combustion of fuel blends but are limited in predicting emissions and exhaust gas composition. A more common approach is the use of a two-zone combustion model with one zone dedicated to the fuel and the second dedicated to the combustion products (Heywood 1988; Guzzella and Onder 2009; Stoumpos et al. 2020; Coraddu et al. 2021). These models can estimate most emissions, but often do not include the formation of No_x since two-zone combustion models are unable to predict local hot spots in the cylinder. Nevertheless, some authors have succeeded in predicting NO_x-formation with these models, e.g. Maroteaux and Saad (2015). Alternatively, a multi-zone model can be employed, accounting for variations in fuel concentration and temperatures within the cylinder without using a complex 3-D model (Verhelst and Sheppard 2009; Kumar et al. 2013; Raptotasios et al. 2015). However, implementing this model still requires a significant amount of computational resources. The highest accuracy is achieved with 3-D/CFD models, which can produce results with nearly no deviation (Coraddu et al. 2021), but are limited to investigate parts of the engine, for example, the combustion chamber with in- and outlet valves (Wang et al. 2020), or even more focussed, for instance, on spray and combustion patterns (Wei et al. 2017; Zhou et al. 2019), but rarely the entire engine. Moreover, the challenge with CFD is the validation of the detailed underlying mechanisms, which requires specific experiments with regulated combustion chambers with optical access.

While emissions formation is dictated by the in-cylinder process, the dynamic response characteristics are predominantly dictated by the turbocharger and gas exchange path dynamics. Understanding and predicting the dynamic response characteristic is essential, considering the following two aspects. First, engine speed and load changes can cause excessive exhaust gas temperatures and steep temperature gradients, accelerating component wear and reducing fatigue life and increasing maintenance burden. Additionally, values for temperature, pressure and supply of fresh air might temporarily exceed the limits for a stable combustion process, causing loss of power and excessive emissions.

The dynamic response characteristic of turbocharged engines is dominated by the performance of the turbocharger (Zinner 1975; Watson and Janota 1982; Baines 2005). The turbocharger's capacity to spin up quickly, driven by the hot exhaust gases, and deliver a higher mass flow of air with increased charge air pressure defines the engine's ability to recover from engine load and speed changes. Ultimately, the maximum available torque strongly depends on the maximum fuel injection, which is limited by the available air mass in the cylinder for complete combustion. Therefore, predicting the turbocharger dynamics is essential to modelling the gas-exchange path of every dynamic engine model. To predict the coupling between exhaust gas flow and supply of fresh air, thus predicting the pressure in the inlet receiver (charge air pressure) with respect to the pressure and temperature in the exhaust receiver, performance characteristics for the compressor and turbine are needed. These performance characteristics describe the relations of mass flow, pressure ratio, rotational speed and isentropic efficiency of the compressor and turbine. They are normally presented as a performance map, see Figure 12. From these relations, the turbine and compressor operating points can be determined, as described in Section 3.4.

Usually, the performance maps for compressor and turbine are determined by the turbocharger manufacturer either by measuring the performance on a dedicated test-bench (Nickel and Grigoriadis 2008; Pucher and Zinner 2012; Mai and Bolz 2015) or with dedicated CFD-simulations (Zellbeck et al. 2013; Boose 2014) and provided to engine manufacturers and system integrators. However, for industrial and marine applications, turbochargers are often designed for a specific engine type or series, and their performance characteristics are kept confidential to gain a competitive advantage. As a result, these performance maps are often unavailable to researchers and engineers investigating integrated power generation plants or marine propulsion systems rather than developing engines.

Several methods have been developed to address this shortfall and predict performance maps with limited input data. For a comprehensive overview, see the review by Galindo et al. (2016) or the extensive introduction of El Hameur et al. (2024). An early attempt to extrapolate performance maps by fitting parabolic curves to the speed lines was introduced by Jensen et al. (1991) and extensively investigated by Moraal and Kolmanovsky (1999). Several other methods exist to extrapolate the performance maps. Although these methods are relatively simple to implement, they rely on at least partial availability of performance maps for extrapolation. Furthermore, they may overlook fundamental principles of turbo-machinery during the scaling process (Swain 2005).

Other methods, therefore, include fundamental principles for the extrapolation, for example, the method proposed by El Hadef (2014), Alternatively, the performance maps can be derived by fundamental principles, some geometric properties, and design point parameters, for example, the methods introduced by Casey and Robinson (2013). The authors present a method to derive the polytropic efficiency and the work coefficient from the flow coefficient and tip-speed Mach number given in the design point of a compressor stage. Speed lines are described with elliptic curves, and the different curvatures are predicted before and after the maximum efficiency point. The method has been improved and refined for different applications (Casey and Rusch 2014; Casey and Robinson 2023) or modified and extended by other researchers, e.g. Al-Busaidi and Pilidis (2015) and Arifin et al. (2018). A similar approach is suggested by Fatsis et al. (2021), describing the speed lines with the complementary error function.

A different approach has been developed by Stapersma (2019), assuming a quadratic dependence between the pressure coefficient and the enthalpy coefficient. This approach is a continuous development and improvement of the theory developed by Gašparović and Stapersma (1973) for staged axial turbo-machinery, allowing for a single set of equations predicting compressor and turbine performance. The sign of a single parameter enabled this method to predict the performance of either a compressor or turbine. The primary focus of Stapersma was integrating his method into a sophisticated mathematical description of the complete diesel engine (Stapersma 2010). Most of the mentioned methods rely on the normalisation of rotational speed, flow, and pressure to fit the data into a wide range of compressors and turbines.

Besides the turbocharger, the flow of fresh air and exhaust gases are also affected by the pipe and volume elements before and after the combustion chamber. Pipes elements, especially non-straight elements like elbows and T-pieces, cause turbulent flows and thus pressure losses. Within pipe elements, the momentum balance can be solved to capture the acceleration and deceleration of the flow. Equilibrium of the momentum balance is normally achieved very fast and the inertial effects on the dynamics of the flow can therefore often be neglected. Pipe elements are consequently often reduced to a simple pressure loss or omitted at all. In contrast, volume elements introduce storage effects of the flow due to the time delay needed to pressurise these elements. Volume elements require solving the mass balance and require significantly more time to reach equilibrium. While

these effects play a minor role for simple turbocharged engines, they dominate the dynamic response characteristic of naturally aspirated engines and can be significant for turbocharged engines with a more complex gas path, including exhaust gas recirculation (EGR), blow-off and bypass valves.

Different simulation approaches can be distinguished to predict and investigate the gas exchange path. Linear and quasi-steady approaches model the gas path as a set of coupled restrictions (Benson et al. 1973; Hendricks 1989; Rakopoulos et al. 2007). Implementing these models for the gas-exchange is very simple, requires very little computational effort and calibration parameters can be extracted from limited measurement data. However, these approaches neglect any dynamic effects of the gas flow, resulting in large errors in the dynamic response characteristics. More insights into the dynamic response characteristics of the gas path are provided with filling-and-emptying models (Zinner 1975; Rakopoulos et al. 2007; Pucher and Zinner 2012; Kolmanovsky et al. 2022). In this approach, manifolds and receivers in the inlet- and exhaust parts are represented by volume elements, linked by resistance elements (Horlock and Winterbone 1986). The dynamic storage effects of the gas path are considered with the conservation of mass and energy for every volume element, but the inertial effects of unsteady flow in the interconnecting piping and resulting pressure waves are neglected. To study the generation and propagation of these pressure waves, wave action models have been developed (Benson 1983; Winterbone et al. 2001; Rakopoulos and Giakoumis 2006; Stockar et al. 2013). The wave action model, also referred to as the gas dynamic model, can predict inertial effects of the unsteady flow on the turbocharger and should be implemented when pulsed turbocharging systems are investigated (Watson and Janota 1982; Baines 2005). The highest accuracy is achieved with 3-D/CFD models, requiring significant computational resources.

While several approaches are available to predict the dynamic response characteristics of internal combustion engines, most authors do not explicitly evaluate the achieved model accuracy for the steady state performance and dynamic response separately. Investigating the dynamic performance of marine propulsion systems in waves or with slow manoeuvring, resulting in a smooth dynamic response, researchers often tend to implement a quasi-steady approach for the gas exchange model (Van Spronsen and Tousain 2001; Oleksiy and Masashi 2010; Theotokatos 2010; Altosole and Figari 2011; Mizythras et al. 2018; Ghaemi and Zeraatgar 2021). If fast load changes on marine generator sets and acceleration manoeuvres of complete vessels are considered, simulating the gas exchange with the filling-and-emptying approach is more common (Benvenuto and Campora 2002; Schulten 2005; Altosole et al. 2017; Tadros et al. 2022; Acanfora et al. 2022). However, the quasi-linear approach is also used, often due to the limited availability of measurement data and turbocharger data (Geertsma et al. 2017; Rusman 2018). For automotive applications with very fast dynamics and switching of valves in the gas path (for example, EGR, blow-off, or bypass valves), the filling-and-emptying approach is often implemented (Heywood 1988; Payri et al. 2002; Wahlström and Eriksson 2010; Chauvin et al. 2011; Casoli et al. 2014; Maroteaux and Saad 2015; Reß et al. 2015), but models relying on the wave action model do exist as well (Payri et al. 1999; Galindo et al. 2007; Costall 2007; Stockar et al. 2013).

3. Model development

3.1. Testbed and data acquisition

For this research, the Caterpillar 3508*A* high-speed, 4-stroke, spark-ignited gas engine of the engine laboratory of the Netherlands Defense Academy (NLDA) in Den Helder was used as a benchmark. This engine is currently running on natural gas from the grid but has run on methanol and different blends of NG with hydrogen in the past (Sapra et al. 2019; Bosklopper et al. 2020) and is, therefore, a suitable representative for a marine spark-ignited engine able to run on alternative fuels. All relevant engine parameters are given in Table 1 and the engine testbed is displayed in Figure 1.

Figure 1. Engine testbed at the NLDA in Den Helder.

Table 1. Engine parameters Caterpillar 3508B.

Feature	Value
Number of cylinders	8
Rated speed	1500 rpm
Cylinder arrangement	60° V
Rated power	500 kWe
Bore	170 mm
Turbocharger type	Garrett TW6146
Stroke	190 mm
TC quantity	2
Displacement	34.5 L
TC configuration	Parallel
Compression ratio	12:1
Max boost pressure	2.25 bar absolute
Fuel type	Low-calorific natural gas
Injection method	Single point injection before TC
Ignition method	Spark ignited (SI)

All pressure and temperature sensors located in the gas path are read out with a sample time of 200 ms by a coupled National Instruments *cRIO*−9057. The turbocharger speed is assessed with an optical sensor directed at the turbocharger shaft. The in-cylinder pressure is obtained with Kistler 7061*C* non-cooled pressure sensors in cylinders 1, 3, 5, and 7. The pressure sensors are coupled to Kistler 5064*D*/*E*-series charge amplifiers and read out with KiBox and a resolution of 0.1°. An overview of the used sensors is given in Table 2.

3.2. Modelling the in-cylinder process

As discussed in the introduction, the dynamic response characteristics of internal combustion engines are mainly determined by

Table 2. Sensor list.

Feature	Manufacturer	Type
In-cylinder pressure p_{cyl}	Kistler	7061C
Mass flow inlet air $\dot{m}_{in}$	Sierra Instruments	640i VT
Temperature inlet air T_{in}	Sierra Instruments	640i VT
Mass flow fuel $\dot{m}_{fuel}$	Bronkhorst	F-106 CI
Pressure before compressor $p_{comp,in}$	GE Druck	PTX 1400
Pressure after compressor $p_{comp,out}$	GE Druck	PTX 5072
Pressure before throttle p_{ac}	Jumo	dTRANS p30
Pressure inlet receiver p_{ir}	Jumo	dTRANS p30
Pressure before turbine $p_{turb,in}$	GE Druck	PTX 5072
Pressure after turbine $p_{turb,out}$	GE Druck	PTX 1400

components of the gas exchange path. The in-cylinder process is required to determine the exhaust conditions based on the inlet receiver conditions and the requested torque, but will not be the focus of this research. Typically, timescales of the dynamic response characteristics of the gas exchange path are in the order of several seconds, whereas the in-cylinder process of the investigated engine, running at 1500 rpm, takes 80 ms to complete. The in-cylinder process was implemented as a mean value first principle engine model to strike a balance between accuracy and computational efficiency. This approach focuses on predicting averaged in-cylinder parameters, offering a valuable alternative to the detailed simulation of individual combustion cycles.

These averaged parameters are determined using the 6-point Seiliger (1926) cycle, since the Seiliger cycle can be calibrated fairly straightforward with available measurement data, see also (Geertsma et al. 2017; Ding et al. 2018; Sapra et al. 2020). This thermodynamic cycle assumes a perfect gas with homogeneous composition and consists of 5 stages: polytropic compression (1-2), the combustion process split into isochoric combustion (2-3), isobaric combustion (3-4), isothermal combustion (4-5), and polytropic expansion (5-6). The thermodynamic state variables and the energy transfer for the 5 stages of the Seiliger cycle can be derived using the equations presented in Table 3. In this table, the state variables are expressed as V_i, p_i and T_i for the volume, pressure, and temperature at point i. Furthermore, specific work from point i to j is given by w_{ij}, and specific heat is given by q_{ij}.

The Seiliger parameters are represented by a, b, and c, r_c is the effective compression ratio and r_e is the expansion ratio of the polytropic expansion stage between Seiliger point 5 (end of isothermal combustion) to point 6 (opening exhaust valve), which can be derived from overall expansion ratio er:

$$er = \frac{V_6}{V_3} = b \cdot c \cdot r_e \tag{1}$$

Finally, $c_{p,g}$ is the specific heat at constant pressure for the gas mixture, $c_{v,g}$ is the specific heat at constant volume for the gas mixture, n_{com} is the polytropic exponent for compression, and n_{exp} is the polytropic exponent for expansion. From this set of equations, the specific indicated work delivered by the cycle can be determined with

$$w_i = w_{12} + w_{34} + w_{45} + w_{56}, \tag{2}$$

and the specific amount of heat provided to the cycle is determined with

$$q_{in} = q_{23} + q_{34} + q_{45}. \tag{3}$$

The thermodynamic efficiency of the cycle can then be established by

$$\eta_{td} = \frac{w_i}{q_{in}} = \frac{W_i}{Q_{in}}, \tag{4}$$

with Q_{in} the total heat input to the cycle, and W_i the indicated work delivered by the cycle.

The heat supplied to the thermodynamic cycle originates from the combustion of the injected fuel. However, not all the chemical energy stored in the fuel is fully released during combustion, and not all the energy released is effectively transferred to the cycle. This is due to the inherent complexity of the combustion process, which involves multiple simultaneous chemical reactions occurring at varying reaction rates. These reactions are primarily driven by the cylinder's temperature and fuel and oxygen availability. Even in premixed combustion, concentration differences occur within the cylinder. Furthermore, ignition by the spark plug results in a combustion zone and expanding flame front, causing an uneven temperature distribution inside the cylinder. As a result, not all injected fuel is combusted completely and some unburned hydrocarbons, CO and soot are emitted. The combustion efficiency η_{comb} for spark-ignited engines is therefore in the range of 95 to 98% (Heywood 1988), which aligns well with the work of Kiouranakis et al. (2025), stating a combustion efficiency of 97.2 to 97.7%. From the energy released during the combustion, a significant amount is lost to the jacket cooling water by heat transfer through the cylinder head and the cylinder liner and by radiation to the air. Combining these two heat losses results in the following equation

$$Q_{in} = \eta_{comb}\eta_q Q_{fuel}, \tag{5}$$

with η_q the heat input efficiency, and Q_{fuel} the theoretical maximum amount of heat provided by combusting the fuel, which can be determined according to

$$Q_{fuel} = m_f h^L, \tag{6}$$

with m_f the amount of fuel injected, and h^L the lower heating value of the fuel. It is important to note that, unlike the Wiebe function, the Seiliger process models the net heat release. This introduces a fundamental algebraic loop unless the heat input and combustion efficiency are assumed constant, as in the present model. A part of the indicated work delivered by the thermodynamic cycle is required to overcome the friction of all moving engine parts and to drive the necessary engine accessories. The effective work can thus be determined by

$$W_e = \eta_m W_i, \tag{7}$$

with η_m the mechanical efficiency. In the nominal operating point, the mechanical efficiency can reach over 90% (Van Basshuysen et al. 2016), but most mechanical losses are not reduced proportionally with engine load and speed. Consequently, the mechanical efficiency deteriorates quickly under part-load conditions. The total engine efficiency can then be derived combining Equations (4), (5), (6), and (7)

$$\eta_e = \frac{W_e}{Q_f} = \eta_m\eta_{comb}\eta_q\eta_{td} \tag{8}$$

At the end of the expansion stroke and just before opening the exhaust valve, pressure and temperature are given by Seiliger point 6. With the exhaust valve opening smoothly due to the camshaft geometry, exhaust gases are not expanding adiabatically into the exhaust receiver. Instead, the exhaust valve acts as a decreasing throttle for the flow of exhaust gases into the exhaust receiver, and the resulting temperature of the exhaust gases will remain higher than predicted with adiabatic expansion. The temperature of the exhaust gases after the blowdown process in the exhaust receiver can be determined

Table 3. Seiliger cycle equations, based on Geertsma et al. (2017).

Process	Volume V	Pressure p	Temperature T	Specific work w	Specific heat q
(1-2) Polytropic Compression	$\frac{V_1}{V_2} = r_c$	$\frac{p_2}{p_1} = r_c^{n_{com}}$	$\frac{T_2}{T_1} = r_c^{(n_{com}-1)}$	$w_{12} = \frac{R_g(T_2 - T_1)}{n_{com} - 1}$	–
(2-3) Isochoric Combustion	$\frac{V_3}{V_2} = 1$	$\frac{p_3}{p_2} = a$	$\frac{T_3}{T_2} = a$	-	$q_{23} = c_{v,g}(T_3 - T_2)$
(3-4) Isobaric Combustion	$\frac{V_4}{V_3} = b$	$\frac{p_4}{p_3} = 1$	$\frac{T_4}{T_3} = b$	$w_{34} = R_g(T_4 - T_3)$	$q_{34} = c_{p,g}(T_4 - T_3)$
(4-5) Isothermal Combustion	$\frac{V_5}{V_4} = c$	$\frac{p_4}{p_5} = c$	$\frac{T_5}{T_4} = 1$	$w_{45} = R_g T_4 \ln c$	$q_{45} = R_g T_4 \ln c$
(5-6) Polytropic Expansion	$\frac{V_6}{V_5} = r_e$	$\frac{p_5}{p_6} = r_e^{n_{exp}}$	$\frac{T_5}{T_6} = r_e^{n_{exp}-1}$	$w_{56} = \frac{R_g(T_6 - T_5)}{n_{exp} - 1}$	–

according to Zinner Zinner (1975)

$$T_{bld} = T_6 \left[1 - \frac{\kappa_g - 1}{\kappa_g} \left(1 - \frac{p_6}{p_{er}} \right) \right], \tag{9}$$

with κ_g the isentropic exponent for the blowdown process, and p_{er} the pressure in the exhaust receiver. To account for heat lost to the exhaust valve, the isentropic expansion is replaced by polytropic expansion, resulting in an altered equation for the blowdown process

$$T_{bld} = T_6 \left[1 - \frac{n_{bld} - 1}{n_{bld}} \left(1 - \frac{p_6}{p_{er}} \right) \right], \tag{10}$$

with n_{bld} the polytropic exponent for the blowdown process. Utilising this blowdown formula as the sole contributor to the turbine entry temperature limits the model's applicability to four-stroke engines with low or no valve overlap.

3.3. Calibration of the seiliger parameters

The implemented calibration of the Seiliger parameters can be compared to the method derived by Sui et al. (2017), showing that the Seiliger parameters can be described with polynomial functions of engine speed and injected mass of fuel. Since the engine of this research is running at a constant speed, the dependency of the Seiliger parameters on engine speed is neglected, and the degree of the polynomial function is decreased to 2^{nd} order. With sufficient measurement data, a machine learning approach to determine the Seiliger parameters could also be considered, but is not in the scope of this research.

For the calibration of the Seiliger parameters, measurements at 5 different steady state operating points have been obtained. The resulting data, including pressure, temperature, and fuel consumption, are summarised in Table 4, providing a foundation for the calibration process. Pressure traces of 200 combustion cycles on one cylinder bank (cylinders 1, 3, 5, and 7) have been recorded to determine the in-cylinder peak pressure. These pressure traces show significant cycle-to-cycle and cylinder-to-cylinder variation, see Figure 2 for an example of a measurement trace captured in the 500 kW steady state operating point. In order to achieve low NO_x emissions, manufacturers design spark-ignited gas engines to run on very lean air-excess ratios to reduce in-cylinder temperatures. The resulting poor combustion with late ignition, incomplete combustion and occasional misfiring leads to significant variations in the pressure traces. Using the maximum pressure value from these measurements for calibration was considered inappropriate, as it would lead to overestimating the pressure in Seiliger stage 6 and an exaggerated pressure drop during the blowdown process. Instead, the maximum pressure value per cycle of all 200 cycles from all 4 cylinders was averaged and defined as peak pressure for the Seiliger cycle approximation, which corresponds well with the results expected from a mean value model. Conversely, this approach demonstrates that a mean value model is unsuited to predict any cylinder-to-cylinder or cycle-to-cycle variation and cannot be used to establish limits for stable combustion. The averaged pressure trace and the deviation is presented in Figure 3, showing the pressure measurement plotted against the cylinder volume in the 100 kW, 250 kW, and 500 kW steady state operating point.

Figure 3 also shows the Seiliger cycle approximation for the previously mentioned steady state operating points. From this figure, it is also clear that every steady state operating point will require its calibration since the cycle's shape is different for every operating point. The calibration requires determining all the parameters needed to solve the Seiliger cycle equations given in Table 3 and all efficiencies stated in Equation (8). Some parameters can be established directly, whereas others require some reshuffling of equations or an estimated guess. Seiliger parameter a follows directly from the pressure ratio of peak pressure to pressure at the end of the compression stroke. Seiliger parameter b is estimated from the p-V diagram by letting the pressure trace of isothermal combustion coincide with the pressure of the averaged measurement. For this, the fraction of heat added during isobaric combustion is estimated, and the Seiliger parameter b is determined according to

$$X_{cp} = \frac{q_{34}}{q_{in}} = \frac{c_{p,g}(T_4 - T_3)}{q_{in}} = \frac{c_{p,g} T_3 (b - 1)}{q_{in}} \tag{11}$$

After determining Seiliger parameters a and b, Seiliger parameter c follows from

$$q_{in} = q_{23} + q_{34} + q_{45} = q_{23} + q_{34} + R_g T_4 \ln c \tag{12}$$

The polytropic exponents for compression n_{com} and expansion n_{exp} are set to match the average pressure signal's compression and expansion shape for the nominal load point. As a result, losses during compression and expansion in part load are slightly overestimated. For simplicity of the model, the polytropic exponents are set constant for compression and expansion throughout all the load cases. The total engine efficiency can be derived by rewriting Equation (8)

$$\eta_e = \frac{W_e}{Q_f} = \frac{W_e}{m_f h^L} = \frac{1}{\text{sfc} \cdot h^L}, \tag{13}$$

with sfc the specific fuel consumption.

Finally, solving the mechanical efficiency η_m and the heat input efficiency η_q is done iteratively since the measurement results do not allow for a direct calculation of their value. By setting one of the efficiencies, the other one follows from Equation (8). Subsequently, all Seiliger equations can be solved and the thermodynamic state variables determined. Overestimating the mechanical losses and thus underestimating the heat input losses results in excessive heat input

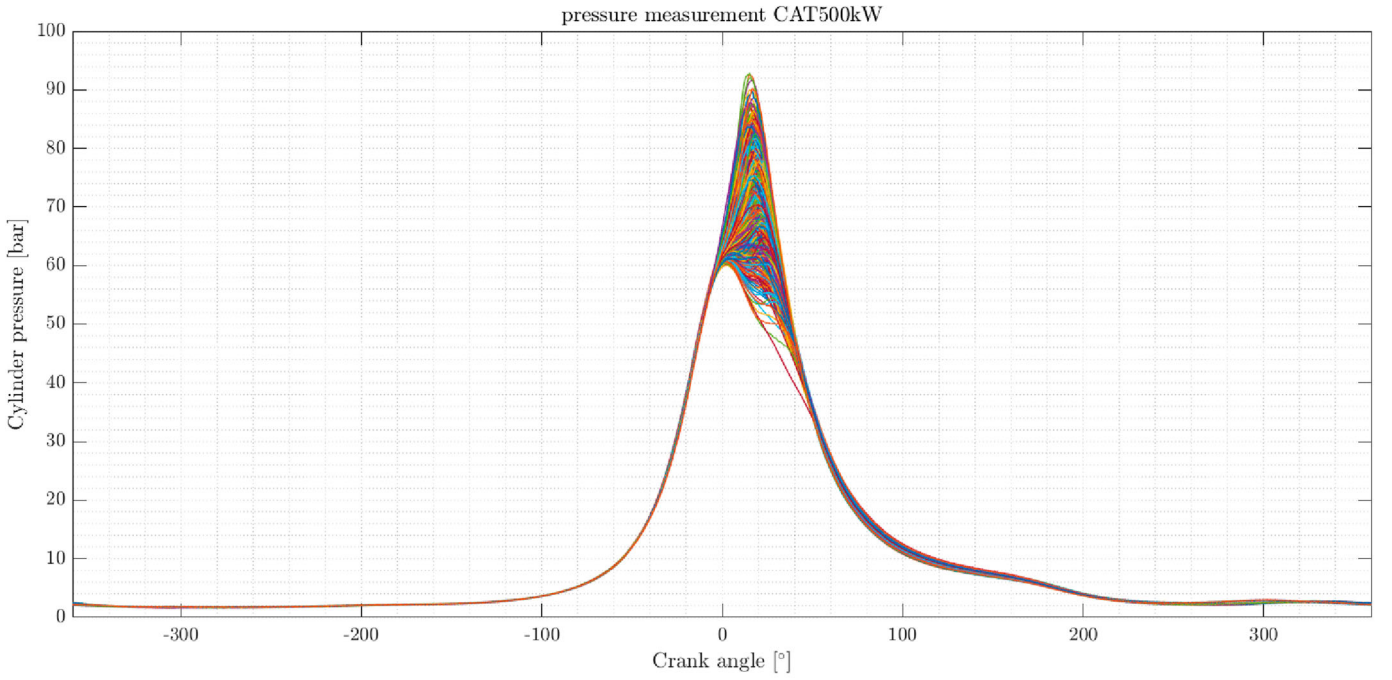

Figure 2. In-cylinder pressure traces, capturing 200 cycles from cylinders 1, 3, 5, and 7 at the 500 kW, 100% MCR steady state operating point.

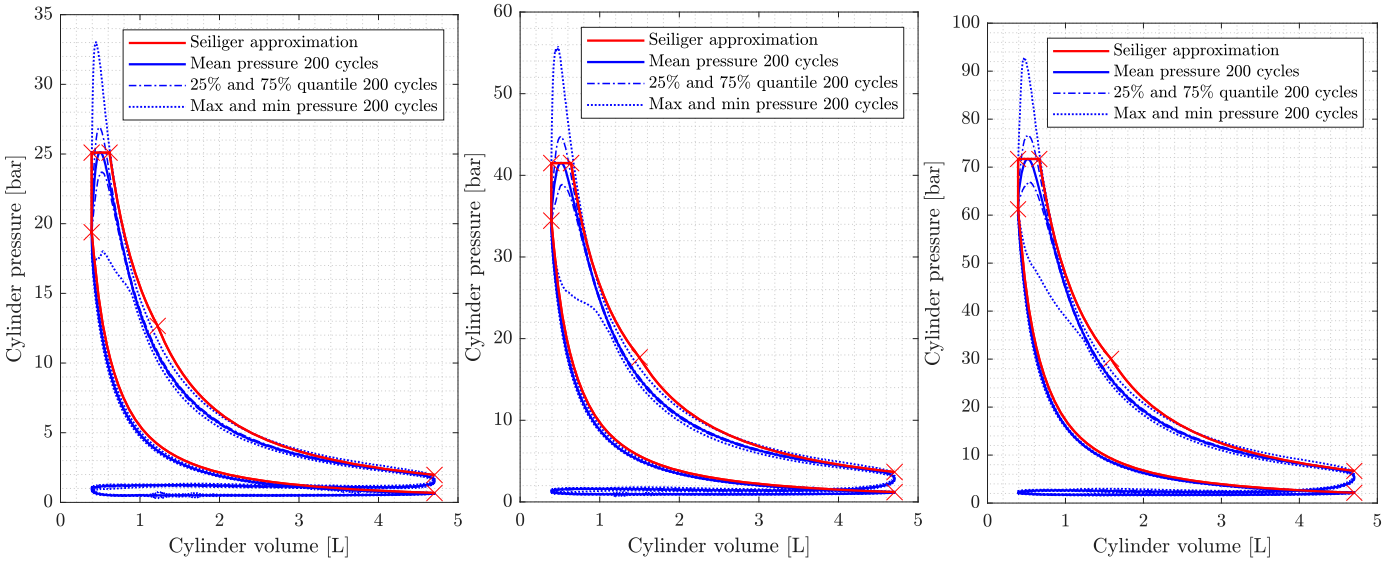

(a) p-V diagram at 100 kW (b) p-V diagram at 250 kW (c) p-V diagram at 500 kW

Figure 3. Seiliger cycle approximation for steady-state operating points at 100 kW, 250 kW, and 500 kW. (a) p-V diagram at 100 kW. (b) p-V diagram at 250 kW and (c) p-V diagram at 500 kW.

Table 4. Measurement data for the calibration of the Seiliger parameters.

Loadpoint	20%	50%	60%	80%	100%
Engine Load	100 kW	250 kW	300 kW	400 kW	500 kW
Pressure Inlet Receiver	67.7 kPa	102.3 kPa	137.6 kPa	176.5 kPa	213.8 kPa
Temperature Inlet Runner	325 K	322 K	321 K	321 K	319 K
Peak Pressure	251 kPa	415 kPa	477 kPa	593 kPa	717 kPa
Pressure Exhaust Receiver	115.7 kPa	146.6 kPa	159.8 kPa	193.2 kPa	234.4 kPa
Temperature Exhaust Runner	825 K	829 K	833 K	846 K	865 K
Specific Fuel Consumption	473 g/kWh	325 g/kWh	309 g/kWh	292 g/kWh	281 g/kWh

Table 5. Calibration values for the Seiliger cycle approximation in the different steady state load points.

Loadpoint	20%	50%	60%	80%	100%
Injected Fuel Mass [g/cyl,cyc]	0.1314	0.2255	0.2257	.3246	0.3906
Mechanical Efficiency	0.64	0.82	0.85	0.89	0.90
Heat Input Efficiency	0.565	0.665	0.675	0.693	0.710
Fraction Heat Isobaric Combustion	0.56	0.56	0.56	0.56	0.58
Seiliger Parameter *a*	1.2948	1.2047	1.2106	1.1733	1.1712
Seiliger Parameter *b*	1.5729	1.6324	1.6372	1.6634	1.6946
Seiliger Parameter *c*	1.9822	2.3450	2.3444	2.5176	2.3853

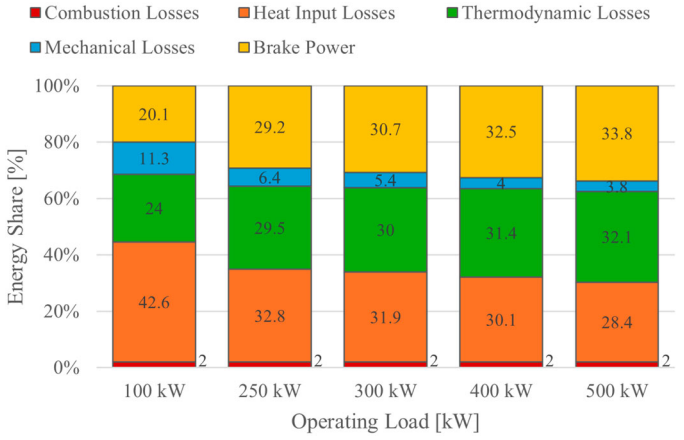

Figure 4. Energy share across load points.

to the cycle. Since Seiliger parameters *a* and *b* are fixed, the isothermal combustion phase is extended, causing temperature T_6 to rise and overestimating T_{bld}. In that case, the estimated efficiency is adjusted and all Seiliger equations need to be solved again until T_{bld} agrees with the measurements.

The results of the calibration process are summarised in Table 5. Using the identified values of mechanical efficiency, heat-release efficiency, and the Seiliger parameters *a*, *b*, and *c*, the in-cylinder combustion process is characterised at the five calibration operating points. From these calibrated values, the breakdown of the energy share can be derived, as printed in Figure 4. Compared with the Heat Release Rate (HRR) analysis performed by Kiouranakis et al. (2025), the present approach may slightly under-predict mechanical losses and over-predict heat input losses, but the total engine efficiency agrees. If an HRR analysis is available in an early stage, the obtained efficiency breakdown could be used as an input to the Seiliger parameter calibration.

The dynamic simulation model must ultimately predict the engine's response not only at these five calibration points but throughout the entire operating envelope. This requires estimating mechanical efficiency, heat-release efficiency, and Seiliger parameters *a*, *b*, and *c* for all possible operating conditions. Following the approach of Geertsma et al. (2017), a relationship between heat release and the injected-fuel mass can be identified. Figure 5 demonstrates this relationship by plotting the calibrated Seiliger parameters against the normalised fuel flow. Similar trends are evident for both mechanical efficiency and heat-release efficiency. These relationships are critical because they enable continuous estimation of combustion characteristics across the entire operating envelope without requiring additional experimental calibration points. By linking Seiliger parameters and efficiencies directly to normalised fuel flow, the model can predict engine performance and thermal behaviour for any setpoint used by the controller. To enable continuous prediction of the in-cylinder combustion process, these dependencies were fitted with second-degree polynomial functions, also shown in Figure 5. With these polynomial relations, the combustion model can now estimate engine efficiency, peak pressure, and exhaust conditions directly from the fuel-flow set-points provided by the engine controller.

3.4. Gas path modelling

As the introduction mentions, different approaches to model the gas path exist. Within this research, we focus on developing a fast mean-value model that is suitable for control purposes and integrated system simulations. Therefore, computationally expensive CFD simulations are not considered, nor are 1-D flow models or wave action models. These models require many geometric parameters of the investigated gas path, which are often unavailable. Dedicated software packages exist to set up and run these models, for example, GT-Power [1] (1-D flow models) or Ricardo Wave [2] (wave action models).

For this research, three different possibilities for setting up the gas path model according to the filling-and-emptying approach will be compared. These approaches can be implemented with limited geometric parameters of the gas path and set up within a standard numeric computing environment, such as MATLAB/Simulink, which can be directly coupled to the in-cylinder process model.

3.4.1. 3 control volumes with full turbocharger

The filling and emptying approach considers several flow receiving or volume elements interconnected by flow control or resistance elements, according to Horlock and Winterbone (1986). With these volume and resistance elements, temperature, pressure, and mass flow of air/exhaust gas of all physical manifolds present in the gas path can be established. In principle, the number of volume elements can be increased to consider even the smallest manifolds in the gas path. Since this increases the model's complexity and computational costs, a trade-off should be made in the number of volume elements. According to the authors, the maximum number of volume elements implemented in a calibrated model is six (Sui et al. 2022). This study considers only the three largest volume elements: the air cooler, the inlet receiver, and the exhaust receiver. Implementing additional volume elements would increase the computational cost of the model, with limited effect on the results due to the negligible size of the remaining volume elements in the gas exchange path. In Figure 6, the implemented volume elements are represented by circles and the resistance elements by rectangles. For every volume element, the conservation of mass is applied, and by considering the ideal gas law, the pressure within the volume element is determined, according to:

$$\frac{\mathrm{d}p}{\mathrm{d}t} = \frac{RT}{V}\frac{\dot{m}_{in} - \dot{m}_{out}}{\mathrm{d}t}, \tag{14}$$

where $\dot{m}_{in}$ and $\dot{m}_{out}$ are the mass flows into and out of the volume element, T is the temperature within the volume element, R is the gas constant of the gas mixture in the volume element and V is the volume of the volume element. The necessary input values of mass flow and temperature for the volume elements are determined within the resistance elements.

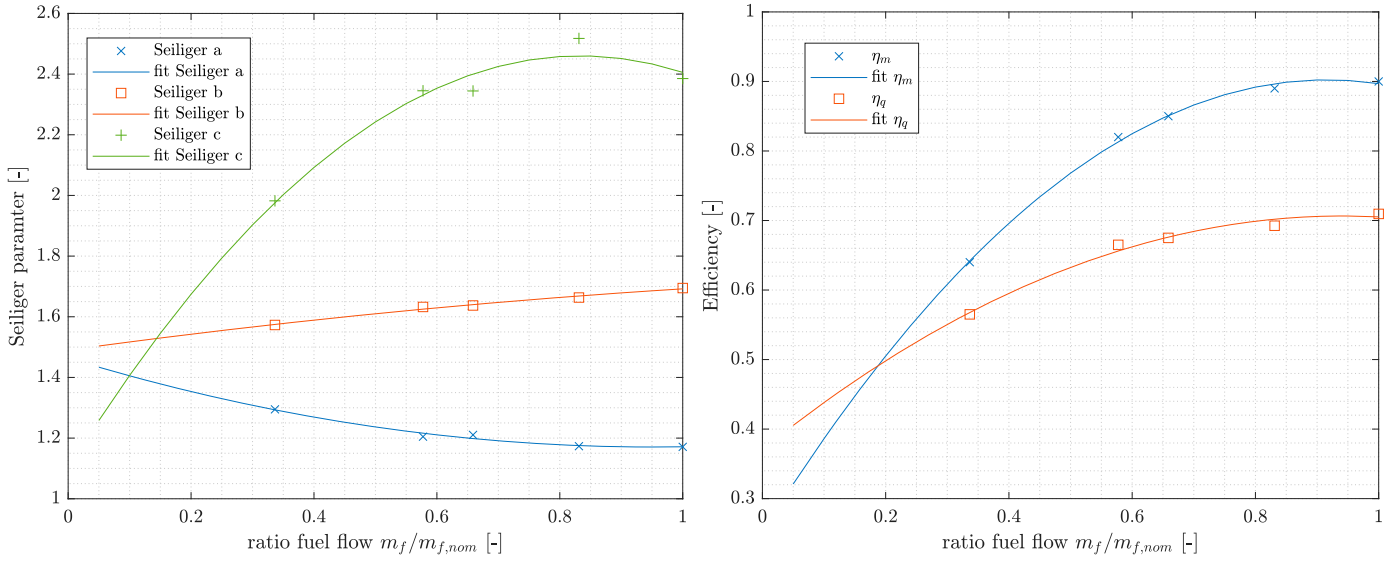

Figure 5. Polynomial fit of Seiliger parameters a, b, c, as well as mechanical efficiency η_m and heat release efficiency η_q for different steady state load points, expressed as dimensionless fuel flow.

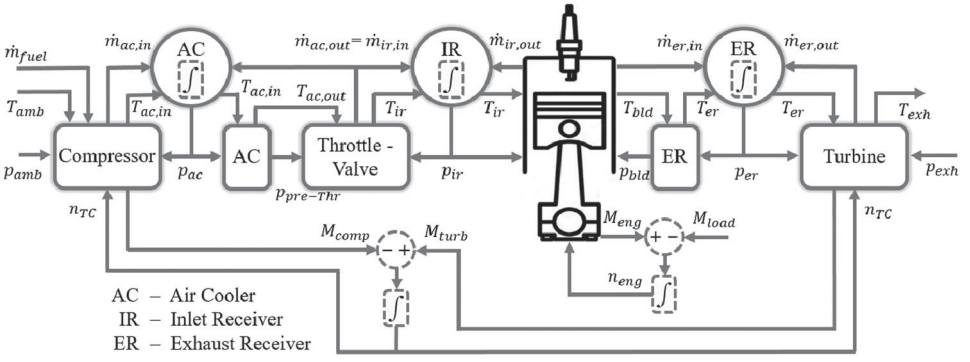

Figure 6. Block diagram of the model with the gas-path represented by 3 control volumes and a full turbocharger model.

The investigated gas engine incorporates a throttle valve for engine speed control. A throttle valve is not used in marine CI engines but is common in the simulation of automotive SI engines (Eriksson et al. 2002; Reß et al. 2015) to control the mass flow of air (or premixed air-fuel) forced into the cylinders, ensuring the engine speed is kept at the desired value. In parallel, fuel flow is controlled by an independent controller, ensuring the right air-excess ratio is maintained. The throttle valve is implemented as a throttle valve with variable throat area according to Heywood (1988), with the opening area A_{th} given by

$$\frac{4A_{th}}{\pi D^2} = \left(1 - \frac{\cos\psi}{\cos\psi_0}\right) + \frac{2}{\pi}\left[\frac{a}{\cos\psi}(\cos^2\psi - a^2\cos^2\psi_0)^{1/2} + \frac{\cos\psi}{\cos\psi_0}\sin^{-1}\left(\frac{a\cos\psi_0}{\cos\psi}\right) - a(1-a^2)^{1/2} - \sin^{-1}a\right], \tag{15}$$

with ψ the opening angle, ψ_0 the throttle plate angle of the closed throttle and a the throttle shaft to throttle bore ratio. The mass flow rate through the throttle can then be determined by

$$\dot{m}_{th} = \frac{C_D A_{th} p_0}{\sqrt{RT_0}}\left(\frac{p_T}{p_0}\right)^{1/\gamma}\left[\frac{2\gamma}{\gamma-1}\left(1 - \frac{p_T}{p_0}\right)^{(\gamma-1)/\gamma}\right]^{1/2}, \tag{16}$$

where p_0 and T_0 are pressure and temperature before the throttle, p_T is the pressure after the throttle and C_D is the throttle discharge coefficient. For operation over the complete operating envelope, the discharge coefficient can be implemented with a continuous fit, according to:

$$C_D(\psi) = a_{C_D} * \psi^2 + b_{C_D} * \psi + c_{C_D} \tag{17}$$

In case the flow is choked through the nozzle ($p_T/p_0 > 0.582$), the mass flow through the nozzle reduces to

$$\dot{m}_{th} = \frac{C_p A_{th}\rho_0}{\sqrt{RT_0}}\gamma^{1/2}\left(\frac{2}{\gamma+1}\right)^{(\gamma+1)/2(\gamma-1)}, \tag{18}$$

where C_p is the discharge coefficient in choked condition and ρ_0 is the gas density before the throttle.

The complete turbocharger model consists of the compressor and turbine resistance elements coupled by the turbocharger shaft's rotational speed. The compressor's delivered mass flow and isentropic efficiency are obtained from the compressor performance map. The temperature after the compressor can be derived from

$$T_{comp,out} = T_{comp,in} + \frac{T_{comp,in}}{\eta_{is,comp}}\left[(\pi_{comp})^{\frac{\kappa_a-1}{\kappa_a}} - 1\right], \tag{19}$$

with $T_{comp,in}$ the temperature before the compressor, π_{comp} the compression ratio and $\eta_{is,comp}$ the isentropic efficiency of the compressor.

The required torque to drive the compressor is given by

$$M_{comp} = \frac{c_{p,a}\dot{m}_{comp}(T_{comp,out} - T_{comp,in})}{n_{TC}}, \tag{20}$$

where m_{comp} is the mass flow delivered by the compressor and n_{TC} is the rotational speed of the turbocharger shaft. Analogous to the compressor, the swallowed mass flow and the isentropic efficiency of the turbine are obtained from the turbine performance map. The temperature after expansion can be determined by

$$T_{turb,out} = T_{turb,in} - \frac{T_{turb,in}}{\eta_{is,turb}}\left[1 - \frac{1}{(\pi_{turb})^{\frac{\kappa_g - 1}{\kappa_g}}}\right], \tag{21}$$

in which $T_{turb,in}$ is the temperature before the turbine, π_{turb} is the expansion ratio over the turbine and $\eta_{is,turb}$ is the isentropic efficiency of the turbine. The delivered torque by the turbine M_{turb} is given by

$$M_{turb} = \frac{c_{p,g}\dot{m}_{turb}\eta_{is,turb}(T_{turb,in} - T_{turb,out,is})}{n_{TC}}, \tag{22}$$

where m_{turb} is the mass flow swallowed by the turbine and $T_{turb,out,is}$ is the temperature after the turbine considering isentropic expansion, as follows

$$T_{turb,out,is} = T_{turb,in} - T_{turb,in}\left[1 - \frac{1}{(\pi_{turb})^{\frac{\kappa_g - 1}{\kappa_g}}}\right]. \tag{23}$$

Finally, the turbocharger shaft speed is determined by considering the equation of motion

$$\frac{\mathrm{d}n_{TC}}{\mathrm{d}t} = \frac{\eta_{m,TC}M_{turb} - M_{comp}}{2\pi J_{TC}}, \tag{24}$$

with $\eta_{m,TC}$ the mechanical efficiency of the turbocharger and J_{TC} the turbochargers polar moment of inertia. The polar moment of inertia was obtained by comparing the turbocharger to known turbochargers with similar compressor and turbine wheel sizes.

3.4.2. 1 control volume with full turbocharger

The gas path can be further simplified by reducing the number of control volumes. This results in a reduction in the number of differential equations to be solved, thus decreasing the computational effort and calibration complexity of the model. In most engines, the inlet receiver is the largest physical manifold in the gas path. Lumping together the capacitative effects of all other manifolds in the inlet receiver will, therefore, result in the smallest overall error on the dynamic response characteristic. Additionally, since the in-cylinder process relies on the inlet receiver parameters as initial conditions, the inlet receiver dynamics also greatly influence the dynamic response characteristics. The block diagram of this simplified approach is presented in Figure 7. In this case, the air cooler and exhaust receiver are implemented with a simple pressure loss and temperature decrease.

Unfortunately, by omitting the volume element of the exhaust receiver the temperature after the blowdown process as reported in Equation (10) cannot be solved analytically without iteration. This equation will now contain the two unknown variables, T_{bld} and p_{er}. The equilibrium pressure in the exhaust receiver is therefore estimated considering the air swallow characteristics of the turbine, according to Stapersma (2010) and Geertsma et al. (2017).

$$p_{er} = \sqrt{\frac{(\dot{m}_{air} + \dot{m}_{fuel})^2 R_g T_{er}}{\alpha_Z^2 A_{eff}^2} + p_{exh}^2}, \tag{25}$$

with α_Z the effective turbine area decrease coefficient equal to one for a constant pressure turbocharger, A_{eff} the effective turbine cross-section area, and p_{exh} the back pressure in the exhaust after the turbine. The effective turbine cross-section area is determined in the nominal condition and kept constant in all other operating conditions, which is valid if the pressure drop across the turbine remains constant (Pucher and Zinner 2012). Considering the decreasing back pressure in the exhaust for part-load, the pressure drop across the turbine will decrease slightly. This results in an error on the effective turbine cross-section area with a maximum deviation of about 5% at idle load. Figure 8 compares predictions based on constant and variable A_eff against the measured exhaust receiver pressure in 6 operating point. Using a constant A_eff reduces accuracy slightly, with the largest deviations occurring in the medium power range.

3.4.3. 1 control volume with simplified turbocharger

The performance maps necessary to set up a full turbocharger model are often unknown. The performance maps can be predicted if sufficient measurement data and some of the turbocharger parameters are available. In Section 3.5, two different methods to predict these maps are introduced, and the performance maps are derived accordingly. However, if insufficient data is available, the turbocharger can be simplified by introducing the turbocharger power balance, according to Zinner (1975) and Pucher and Zinner (2012)

$$\pi_{comp} = \left[1 + \frac{\dot{m}_{turb}}{\dot{m}_{comp}} \cdot \frac{c_{p,g}}{c_{p,a}} \cdot \frac{T_{turb,in}}{T_{comp,in}} \cdot \eta_{TC} \cdot \left(1 - (\pi_{turb})^{\frac{\kappa_g - 1}{\kappa_g}}\right)\right]^{\frac{\kappa_a - 1}{\kappa_a}}, \tag{26}$$

with η_{TC} the total efficiency of the turbocharger, thus combining the mechanical efficiency, isentropic efficiency of the compressor and isentropic efficiency of the turbine of the previous section in one parameter. The total efficiency of the turbocharger is not constant for all load points but is a function of the turbocharger speed and pressure ratio. Since the simplified approach does not predict the turbocharger speed, the efficiency is determined with a quadratic function of the compressor pressure ratio, analogous to Geertsma et al. (2017)

$$\eta_{TC} = a_{TC} \cdot \left(1 - \frac{\pi_{comp}}{\pi_{comp,nom}}\right)^2 + b_{TC} \cdot \left(1 - \frac{\pi_{comp}}{\pi_{comp,nom}}\right) + c_{TC}, \tag{27}$$

with $\pi_{comp,nom}$ the compressor pressure ratio in the nominal operating point, and a_{TC}, b_{TC}, and c_{TC} the polynomial coefficients. To capture the effect of the turbocharger's rotational inertia, a first-order time delay on the compressor outlet pressure $p_{comp,out}$ can be implemented by

$$\frac{\mathrm{d}p_{comp,out}}{\mathrm{d}t} = \frac{p_{comp,out,s} - p_{comp,out}}{\tau_{TC}}, \tag{28}$$

with $p_{comp,out,s}$ the static compressor outlet pressure, as determined with Equation (26) and τ_{TC} the turbocharger time constant. To determine the turbocharger time constant, a dedicated measurement of a single load step was made, and the time constant was calibrated accordingly. The block diagram with the simplified turbocharger model is presented in Figure 9.

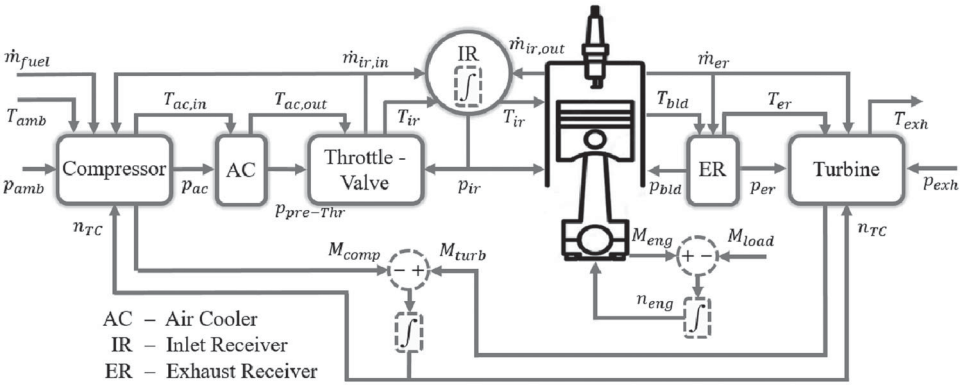

Figure 7. Block diagram of the model with the gas-path represented by 1 control volume and a full turbocharger model.

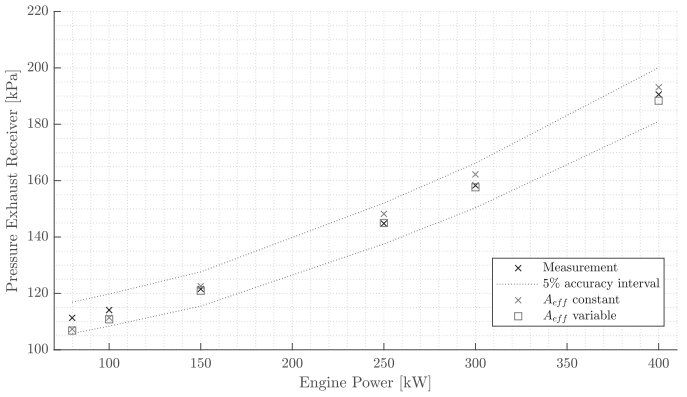

Figure 8. Exhaust reveiver pressure prediction with constant and variable effective turbine cross-section area A_{eff}.

3.5. Deriving turbocharger performance data

This research will predict compressor performance using the methods developed by Casey and Robinson (2013) and by Stapersma (2019). While the method proposed by Casey & Robinson requires some geometrical parameters of the investigated compressor, which might not always be available, the method proposed by Stapersma relies on flow coefficients only, effectively reducing the required model calibration parameters. Besides the geometrical and model parameters, both methods require several properties of the design point, which is defined as the operating point with the highest efficiency. To determine the design point of the compressor, measurements of rotational speed, mass flow, pressure before and after the compressor, and temperature before and after the compressor were taken in 12 different load points of the engine.

The method of Casey and Robinson (2013) proposes normalisation of the rotational speed and flow to predict the development of efficiency and work. Casey & Robinson suggest the use of two elliptic curves to predict the efficiency above and below the design point. For every non-dimensional impeller speed, these curves are determined with a set of pre-defined shape parameters. The authors present these shape parameters by examining a large set of compressor maps. Besides the design point parameters, this method requires determining the four key nondimensional parameters:

- The global volume flow coefficient Φ, given by

$$\Phi = \frac{\dot{V}}{u_2 D_2^2}, \tag{29}$$

with $\dot{V}$ the volume flow rate through the compressor, u_2 the impeller blade tip speed, and D_2 the impeller blade tip diameter.

- The stage work coefficient λ, given by

$$\lambda = \frac{\Delta h}{u_2^2}, \tag{30}$$

with Δh the difference in specific enthalpy between compressor inlet and outlet.

- The tip-speed Mach number M, established with

$$M = \frac{u_2}{a_1}, \tag{31}$$

with a_1 the inlet speed of sound.

- The design point polytropic efficiency η_{pol}, which can be defined as the isentropic efficiency of an elemental stage in the compressor (Saravanamuttoo et al. 2001; Boyce 2011). Since the compressor comprises of just one centrifugal compressor stage, the polytropic efficiency will be set equal to the isentropic efficiency, given by

$$\eta_{pol} = \frac{T_{comp,out,is} - T_{comp,in}}{T_{comp,out} - T_{comp,in}}, \tag{32}$$

with $T_{comp,out,is}$ the isentropic compressor outlet temperature, which can be determined by

$$T_{out,is} = T_{in} \cdot \pi^{\frac{\kappa_a - 1}{\kappa_a}}. \tag{33}$$

The highest estimated compressor efficiency measurement point was chosen as the design condition. The remaining three key nondimensional parameters can be determined by combining the measured properties and the geometrical parameters. The corresponding design condition properties are given in Table A1, Appendix 1, and the choice of model parameters from the suggested range by Casey & Robinson. The resulting performance map with the measured compressor working points is given in Figure 10. For rotational speeds below the design condition, the pressure ratio is slightly underpredicted, and for rotational speeds above the design condition, the pressure ratio is slightly over-predicted.

The method by Stapersma (2019) proposes a linear model for the enthalpy coefficient ψ^* and a quadratic model for the pressure coefficient ε^*. All coefficients marked with an asterisk are normalised, facilitating the scalability of the results. The linear relation between ψ^* and the effective flow coefficient φ^* is derived considering Euler's

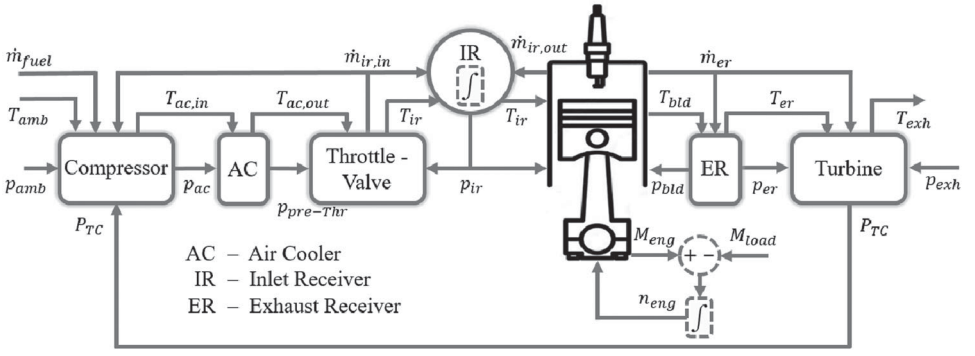

Figure 9. Block diagram of the model with the gas-path represented by 1 control volume and a simplified turbocharger model.

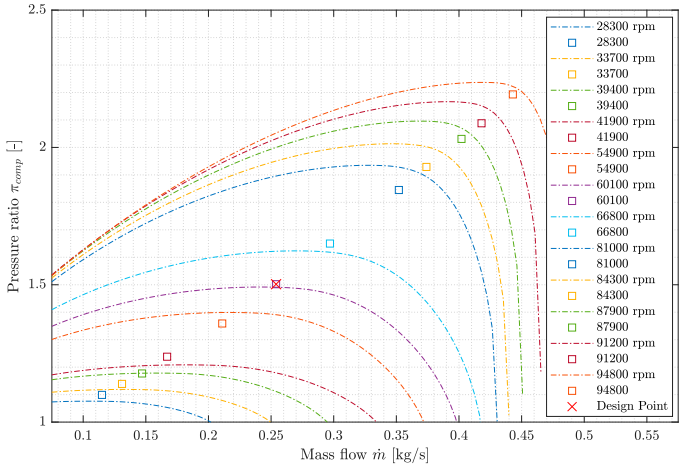

Figure 10. Predicted Compressor Performance Map according to Casey and Robinson (2013), showing the predicted speed lines of the compressor and the measured compressor working points (indicated with a square).

law:

$$\psi^* = \frac{\psi}{\psi_0} = \frac{1 - \varphi_1 \frac{u_1}{u_2} \cot\alpha_1 + \varphi_2 \cot\beta_2}{\psi_0} = 1 + \left(1 - \frac{1}{\psi_0}\right)(\varphi^* - 1), \tag{34}$$

with φ_1 and φ_2 the flow coefficients at rotor entry and exit, u_1 and u_2 the circumferential velocities at rotor entry and exit, α_1 the absolute inlet flow angle, β_2 the relative outlet flow angle, ψ_0 the nominal enthalpy coefficient, and the dimensionless enthalpy change over the stage ψ defined by:

$$\psi = \frac{\Delta h}{u_2^2}. \tag{35}$$

Keeping in mind this definition, the enthalpy coefficient can also be expressed in the temperature change by

$$\psi^* = \frac{1}{\nu^{*2}} \frac{\tau - 1}{\tau_0 - 1}, \tag{36}$$

with τ the temperature ratio across the stage, τ_0 the temperature ratio across the stage in design condition, and ν^* the non-dimensional impeller speed determined by

$$\nu^* = \frac{n}{n_0 \sqrt{\frac{T_{in}}{T_{in,0}}}}, \tag{37}$$

The flow coefficients at rotor entry and exit are defined by

$$\varphi_n = \frac{\nu_{m,n}}{u_2}, \tag{38}$$

where the subscript n indicates either the inlet or outlet position, and $\nu_{m,n}$ represents the axial absolute velocity at the corresponding location. The pressure coefficient ε^* is assumed to be quadratic in flow and speed:

$$\varepsilon^* = 1 + \left(1 - \frac{1}{\psi_0}\right)(\varphi^* - 1) - \frac{1}{\psi_0}(\varphi^* - 1)^2 - \text{sign}(\psi_0)(\nu^* - 1)^2, \tag{39}$$

with the pressure coefficient ε^* defined by

$$\varepsilon^* = \frac{1}{\nu^{*2}} \left(\frac{\pi^{\frac{\kappa-1}{\kappa}} - 1}{\pi_0^{\frac{\kappa-1}{\kappa}} - 1} \right). \tag{40}$$

The relative efficiency η^* is determined by the relation between the enthalpy coefficient and the pressure coefficient:

$$\frac{\varepsilon^*}{\psi^*} = \begin{cases} \eta^*_{comp}, & \text{for a compressor, with } \eta_{comp} = \eta^*_{comp} \cdot \eta_0 \\ \dfrac{1}{\eta^*_{turb}}, & \text{for a turbine, with } \eta_{turb} = \eta^*_{turbine} \cdot \eta_0, \end{cases} \tag{41}$$

Solving the quadratic Equation (39) requires the first three of the four model parameters:

- Sensitivity parameter x, determining the stretch of the predicted map parallel to the φ^*-axis and with respect to the design condition. A wider compressor map allows the compressor to deliver a wider range of mass flow against constant pressure and is typical for compressors with low compression ratios.
- Sensitivity parameter y, determining the stretch of the predicted map parallel to the ν^*-axis and in respect to the design condition. A higher compressor map allows the compressor to deliver a constant mass flow against a wider range of pressure ratios.

- The nominal enthalpy coefficient ψ_0, defined as

$$\psi_0 = \frac{\Delta h_0}{u_{2,0}^2}, \tag{42}$$

with Δh_0 the difference in enthalpy between compressor inlet and outlet in design condition, and $u_{2,0}$ the impeller blade tip speed in design condition. The enthalpy coefficient determines the compressor's loading and thus influences the curvature of the predicted compressor speed lines.

- the nominal Mach number Ma_0, defined by

$$Ma_0 = \frac{v_{m,0}}{\sin\alpha_0 \cdot a_1}, \tag{43}$$

with $v_{m,0}$ the axial absolute fluid velocity at rotor inlet, and α_0 the apparent air angle through the moving impeller. The Mach number indicates the margin between the working point and the maximum mass flow in choking conditions.

With these model parameters, coefficients a, b, and d are defined by

$$\begin{aligned} a &= 1 - \frac{1}{\psi_0} \\ b &= -x \cdot \frac{1}{\psi_0} \\ d &= -y \cdot \mathrm{sign}(\psi_0) \end{aligned} \tag{44}$$

If the performance map is entered from the mass flow side, the pressure can be determined from the quadratic Equation (39) with these coefficients. More often, though, the pressure over the turbocharger is known, and the quadratic equation needs to be solved for the mass flow through the turbocharger. In that case, Equation (39) needs to be rewritten to

$$\varphi^* = \frac{-(a-2b) \pm \sqrt{(a-2b)^2 - 4b \cdot \left[1 - \varepsilon^* - a + b + d \cdot (\nu^* - 1)^2\right]}}{2b} \tag{45}$$

For every non-dimensional impeller speed, the flow coefficient can be expressed by the relative Mach number Ma^* at rotor entry:

$$Ma^* = \varphi_1^* \nu^* \sqrt{\frac{1-q}{1 - q(\varphi^* \nu^*)^2}}, \tag{46}$$

with coefficient q derived from the fourth model parameter by

$$q = \frac{\frac{\kappa-1}{2} Ma_0^2}{1 + \frac{\kappa-1}{2} Ma_0^2}. \tag{47}$$

The relation between the effective flow coefficient and the flow coefficient at rotor entry and rotor exit is defined by

$$\varphi^* = (1-s)\varphi_1^* + s\varphi_2^*, \tag{48}$$

with s the split factor. Reshuffling this equation results in:

$$\varphi_1^* = \frac{\varphi^*}{(1-s) + s\frac{\varphi_2^*}{\varphi_1^*}}. \tag{49}$$

The ratio of $\frac{\varphi_2^*}{\varphi_1^*}$ can be obtained by solving

$$\frac{\varphi_2^*}{\varphi_1^*} = \frac{\pi_0}{\tau_0} \frac{1 + \nu^*(\tau_0 - 1)}{\left\{1 + [1 + d(\nu^* - 1)^2]\nu^{*2}\left(\pi_0^{\frac{\kappa-1}{\kappa}} - 1\right)\right\}^{\frac{\kappa}{\kappa-1}}} \tag{50}$$

The mass flow is limited once chocking conditions are reached, i.e. Ma = 1. This can be achieved by limiting the the relative Ma number Ma^* and the resulting non-dimensional mass flow μ^* with

$$\mu^* = \begin{cases} \dfrac{Ma^*}{\left[(1-q) + q\,Ma^{*2}\right]^{\frac{\kappa+1}{2(\kappa-1)}}}, & \text{if } Ma^* \le Ma^*_{\max} \\ \dfrac{Ma^*_{\max}}{\left[(1-q) + q\,Ma^{*2}_{\max}\right]^{\frac{\kappa+1}{2(\kappa-1)}}}, & \text{otherwise} \end{cases} \tag{51}$$

with $Ma^*_{\max}$ to be determined with

$$Ma^*_{\max} = \sqrt{\frac{\kappa-1}{2}\frac{1-q}{q}}. \tag{52}$$

The mass flow can finally be determined from the non-dimensional (or corrected) mass flow μ^*, given by:

$$\mu^* = \frac{\dot{m}}{\dot{m}_0}\sqrt{\frac{T_{in}}{T_{in,0}}}\frac{p_{in,0}}{p_{in}}. \tag{53}$$

Comparing the two methods, a resemblance in the input parameters can be identified. The definition of the stage work coefficient λ by Casey & Robinson is identical to the definition of the enthalpy coefficient ψ by Stapersma. Furthermore, both methods use the Mach number, but while Casey & Robinson define the Mach number with respect to the impeller tip speed, Stapersma refers to the axial absolute fluid velocity. However, both method require the Mach number to estimate the location of the choking line. Although not required as input parameter, the method by Stapersma defines the flow coefficient φ analogously as the ratio of axial fluid velocity to the circumferential speed of the impeller to predict the location of maximum efficiency for different compressor speed lines.

3.5.1. Compressor model calibration via parameter optimisation

Due to limitations in the available measurement data, the precise location of the peak compressor efficiency could not be directly identified. However, based on prior knowledge and consistency across measurements, it was assumed that the efficiency peak lies along the measured operating line. Notably, the estimated compressor efficiency exhibited only minor variations across the investigated rotational speeds–54,900 rpm, 60,100 rpm, 66,800 rpm, and 81,000 rpm–thus justifying the use of a common parameter set across all operating conditions.

To calibrate the compressor performance model derived from the method of Stapersma, a parameter estimation problem was formulated. The objective was to minimise the discrepancy between the model-predicted and measured compressor pressure ratios across $N = 12$ measurement points. The parameter vector is defined as

$$\boldsymbol{\theta} = \begin{bmatrix} x & y & Ma_0 & \psi_0 & s \end{bmatrix}^\top \in \mathbb{R}^5, \tag{54}$$

where x and y are sensitivity parameters, Ma_0 is the nominal Mach number, ψ_0 is the nominal enthalpy coefficient, and s is the flow split

factor. The optimisation problem is given by:

$$\min_{\boldsymbol{\theta}\in\mathbb{R}^5} \quad J(\boldsymbol{\theta}) = \sum_{i=1}^{N} w_i \left[\pi_{\text{comp}}^{\text{model}}(i;\boldsymbol{\theta}) - \pi_{\text{comp}}^{\text{meas}}(i)\right]^2$$
$$\text{subject to} \quad \boldsymbol{\theta}^{\text{lower}} \leq \boldsymbol{\theta} \leq \boldsymbol{\theta}^{\text{upper}}, \tag{55}$$

where w_i denotes the weight assigned to measurement point i, $\pi_{\text{comp}}^{\text{meas}}(i)$ is the measured compressor pressure ratio, and $\pi_{\text{comp}}^{\text{model}}(i;\boldsymbol{\theta})$ is the corresponding model prediction. The parameter bounds are defined as:

$$\boldsymbol{\theta}^{\text{lower}} = \begin{bmatrix}2.0 & 0.1 & 0.4 & 0.3 & 0.5\end{bmatrix}^\top,$$
$$\boldsymbol{\theta}^{\text{upper}} = \begin{bmatrix}4.0 & 1.5 & 1.0 & 1.0 & 1.0\end{bmatrix}^\top.$$

The optimisation problem described in Equation (55) is a bounded nonlinear least-squares problem. The objective function is continuous and smooth but generally *nonconvex*, as it depends on a nonlinear physical model incorporating thermodynamic relationships, empirical corrections, and operating line assumptions. The lack of analytical gradients–due to embedded empirical components and lookup-based submodels–necessitates the use of derivative-free optimisation strategies.

A suitable approach for this low-dimensional setting is the *Nelder-Mead simplex algorithm*, which is widely used for smooth, unconstrained or mildly constrained nonlinear optimisation. To incorporate the parameter bounds, a quadratic penalty function was added to the objective:

$$J_{\text{pen}}(\boldsymbol{\theta}) = J(\boldsymbol{\theta}) + \mu \sum_{j=1}^{5} \left(\max(0, \theta_j^{\text{lower}} - \theta_j)^2 + \max(0, \theta_j - \theta_j^{\text{upper}})^2\right), \tag{56}$$

where $\mu > 0$ is a user-defined penalty factor (empirically tuned) that enforces the box constraints during the optimisation.

Several alternative strategies could be considered for solving the parameter estimation problem, depending on the trade-off between computational efficiency, robustness, and implementation complexity. Among these, trust-region reflective algorithms–specifically designed for bounded nonlinear least-squares problems–are capable of leveraging numerical derivatives and often exhibit strong local convergence properties. Bayesian optimisation, while well-suited for expensive black-box functions with limited evaluation budgets, may be unnecessarily complex for problems of such low dimensionality. Metaheuristic approaches such as genetic algorithms or differential evolution offer robustness to nonconvexity and multimodality but tend to be less computationally efficient and require careful tuning. Gradient-based methods with bounded constraints, including L-BFGS-B, can also be effective provided that reliable gradient approximations are available through finite differences. However, given the smooth yet non-differentiable nature of the underlying model, the Nelder–Mead simplex algorithm was selected as a practical and robust solution method, offering a favourable balance between implementation simplicity, convergence behaviour, and robustness to noise and irregularities in the objective landscape.

The resulting design condition parameters are presented in Table A1, Appendix 1, and the resulting performance map with the measured compressor working points is given in Figure 11. Both compressor maps, including the predicted efficiency, are plotted in Figure 12.

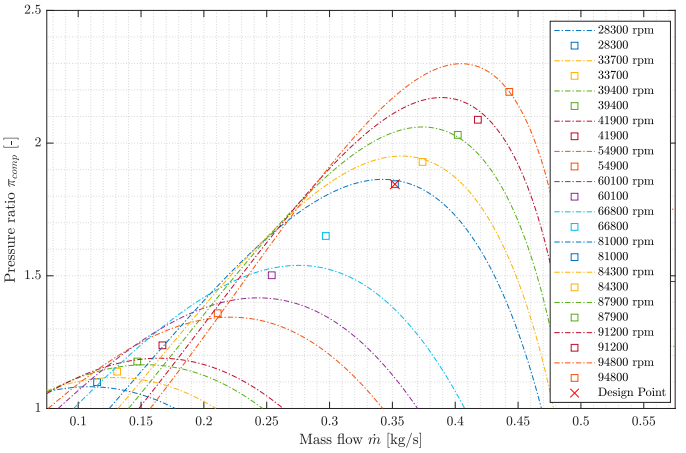

Figure 11. Predicted Compressor Performance Map according to Stapersma (2019), showing the predicted speed lines of the compressor and the measured compressor working points (indicated with a square).

3.5.2. Turbine model calibration via parameter optimisation

Given that the method of Casey & Robinson does not support turbine performance prediction, optimisation of turbine parameters was conducted exclusively using the approach proposed by Stapersma (2019). In the Stapersma framework, turbine performance prediction is enabled by defining four model-specific parameters as well as a full set of design condition parameters. In particular, a negative nominal enthalpy coefficient ψ_0 is used to reflect the turbine expansion process.

To calibrate the turbine model to experimental data, a constrained parameter estimation problem was formulated. The objective was to minimise the discrepancy between the predicted and measured turbine pressure ratios across $N = 12$ operating conditions. The decision variable is the extended parameter vector

$$\boldsymbol{\theta} = \begin{bmatrix}x & y & Ma_0 & \psi_0 & n_0 & \dot{m}_0 & \pi_0\end{bmatrix}^\top \in \mathbb{R}^7, \tag{57}$$

where x and y are sensitivity parameters, Ma_0 and ψ_0 represent the nominal Mach number and nominal enthalpy coefficient, respectively, and n_0, $\dot{m}_0$, and π_0 denote the design rotational speed, mass flow rate, and pressure ratio. For the turbine model, split factor was excluded from the optimisation and set to 0.

The optimisation problem was defined as follows

$$\min_{\boldsymbol{\theta}\in\mathbb{R}^7} \quad J(\boldsymbol{\theta}) = \sum_{i=1}^{N} w_i \left[\pi_{\text{turb}}^{\text{model}}(i;\boldsymbol{\theta}) - \pi_{\text{turb}}^{\text{meas}}(i)\right]^2$$
$$\text{subjectto} \quad \boldsymbol{\theta}^{\text{lower}} \leq \boldsymbol{\theta} \leq \boldsymbol{\theta}^{\text{upper}}, \tag{58}$$

with the bound vectors defined as

$$\boldsymbol{\theta}^{\text{lower}} = \begin{bmatrix}1.0 & 0.1 & 0.5 & -4.0 & 30\,000\,\text{rpm} & 0.1\,\text{kg s}^{-1} & 1.0\end{bmatrix}^\top,$$
$$\boldsymbol{\theta}^{\text{upper}} = \begin{bmatrix}2.0 & 1.0 & 0.9 & -1.0 & 90\,000\,\text{rpm} & 0.5\,\text{kg s}^{-1} & 2.4\end{bmatrix}^\top.$$

Here, $\pi_{\text{turb}}^{\text{model}}(i;\boldsymbol{\theta})$ denotes the model-predicted turbine pressure ratio at operating point i, $\pi_{\text{turb}}^{\text{meas}}(i)$ is the corresponding measured value, and w_i is a weight applied to each residual to reflect measurement relevance or confidence.

The resulting problem is a smooth but nonconvex nonlinear least-squares optimisation over a bounded domain in $\mathbb{R}^7$. Due to the model's nonlinear structure, the absence of analytical gradients, and the moderate dimensionality of the parameter space, a derivative-free optimisation strategy was adopted. As in the compressor case,

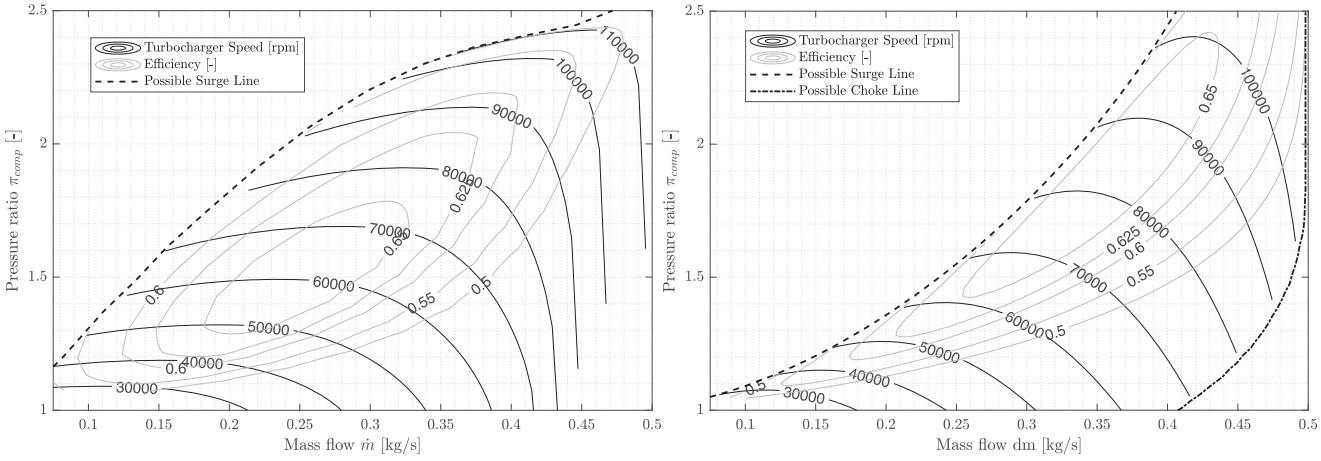

(a) According to Casey and Robinson (2013) (b) According to Stapersma (2019)

Figure 12. Predicted Compressor Performance Maps including efficiency and indication of surge and choke lines. (a) According to Casey and Robinson (2013) and (b) According to Stapersma (2019).

the Nelder–Mead simplex method was used in combination with a penalty formulation to handle box constraints, yielding a penalised objective function:

$$J_{\text{pen}}(\boldsymbol{\theta}) = J(\boldsymbol{\theta}) + \mu \sum_{j=1}^{7} \left(\max(0, \theta_j^{\text{lower}} - \theta_j)^2 + \max(0, \theta_j - \theta_j^{\text{upper}})^2 \right), \tag{59}$$

where $\mu > 0$ is a penalty parameter and $\boldsymbol{\theta}^{\text{lower}}, \boldsymbol{\theta}^{\text{upper}}$ represent the bounds imposed on the parameter vector, as listed in Equation (58).

For comparison, a turbine performance prediction based on the simplified curve-fitting approach proposed by Jensen et al. (1991) was also incorporated. The resulting design condition parameters are presented in Table A1, Appendix 1, and the resulting performance map with the measured turbine working points is given in Figure 13. Compared to the compressor prediction, the turbine prediction resulted in a less accurate fit with the measurement data. The reason for this is three-fold:

(1) The temperature measurements of turbine inlet and outlet temperatures are less reliable compared to the compressor temperature measurements due to the fluctuations in exhaust temperature and the higher heat transfer rates to the water-cooled exhaust receiver walls and the water-cooled turbine housing.
(2) The model determines the non-dimensional impeller speed ν^* with

$$\nu^* = \frac{n}{n_0 \sqrt{\frac{T_{in}}{T_{in,0}}}}, \tag{60}$$

and the non-dimensional (or corrected) mass flow μ^* with

$$\mu^* = \frac{\dot{m}}{\dot{m}_0} \sqrt{\frac{T_{in}}{T_{in,0}}} \frac{p_{in,0}}{p_{in}}. \tag{61}$$

Both equations are sensitive to the turbine inlet temperature and thus sensitive to the measurement error of this temperature.
(3) The investigated turbocharger is old with relatively low compressor efficiency and achievable compressor pressure ratio compared to the rotational speed of the turbocharger. As a result, the pressure ratio over the turbine is even lower due to the construction principle with the throttle valve. The investigated prediction methods struggle to correctly predict the performance of the compressor on the very low pressure ratios, but even more so with predicting the turbine performance in these circumstances.

3.6. Control strategy

The implemented engine control strategy consists of two separate controllers for fuel flow control and engine speed control, see Figure 14. The throttle valve controls the engine speed, forming a controllable restriction on the mass flow of mixed air and fuel from the compressor to the inlet receiver. In the physical controller, set points for the throttle valve are generated by a PID controller with variable gain settings. According to Baan (2025), the relationship between the throttle command, $THR_{actuator,set}$, and the resulting throttle angle, $THR_{angle,set}$, can be represented by a linear mapping for actuator setpoints above 20 percent. This mapping is given by

$$\text{THR}_{\text{angle,set}}\ [\text{deg}] = 0.75\ \frac{\text{deg}}{\%} \cdot \text{THR}_{\text{actuator,set}}\ [\%].$$

In this formulation, an actuator setpoint of 0% corresponds to a fully closed throttle at 0°, while a setpoint of 100% corresponds to a fully open throttle at 75°.

The implemented PID controller uses fixed gain settings for simplifications, according to Table 6. The inertia of the throttle valve has been implemented with a first-order time delay with time constant τ_{THR}.

A TecJet gas valve adjusts the fuel flow, controlling the amount of fuel added to the inlet air before the compressor. The fuel controller estimates the actual air-to-fuel ratio based on the pressure and temperature in the inlet receiver. With tabular values for the desired air-to-fuel ratio, known as the fuel mapping, and the estimated actual air-to-fuel ratio, the TecJet controller determines set points for the gas valve. While setting up the model, no information on the physical fuel controller was available. Therefore, the mass flow of fuel will be directly resolved from the desired air-to-fuel ratio. The controller delay and inertia of the fuel valve were captured with a single first-order time delay with time constant τ_{fuel}.

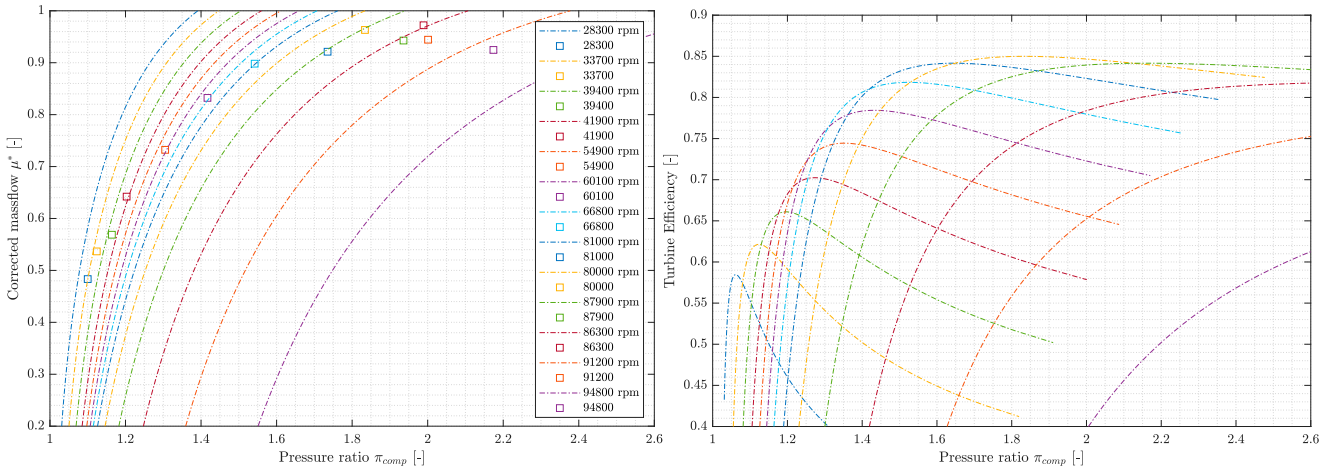

(a) Turbine performance map with measurement points

(b) Efficiency map

Figure 13. Predicted Turbine Performance Map according to Stapersma (2019). (a) Turbine performance map with measurement points and (b) Efficiency map.

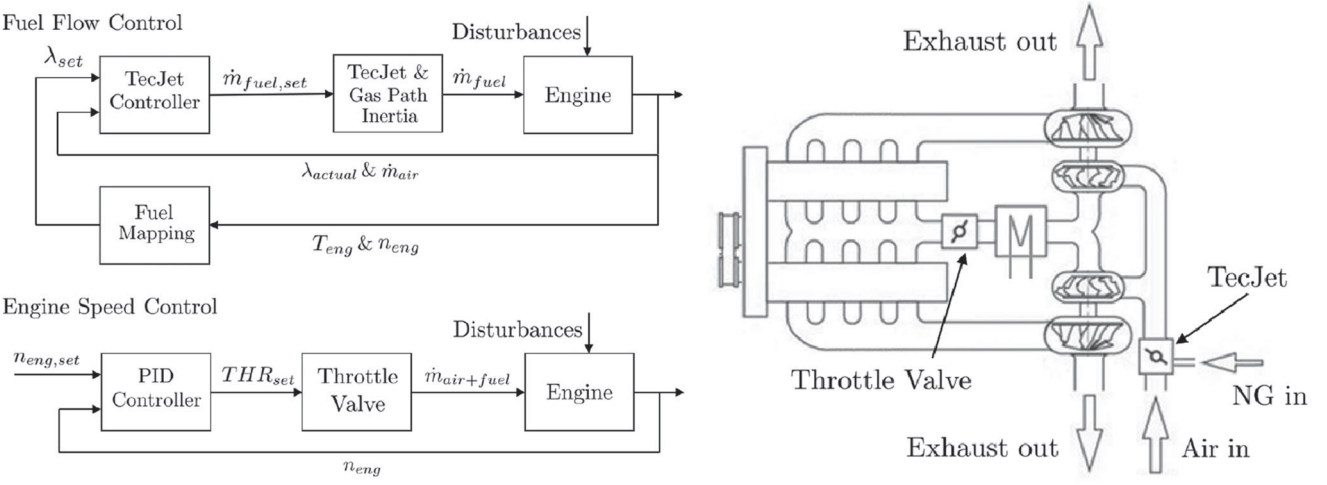

Figure 14. Schematic layout of the engine and controller from Vollbrandt et al. (2023).

The time constants τ_{THR} and τ_{fuel} were determined with a dedicated measurement of one load step, as part of earlier research by Vollbrandt et al. (2023). However, assumptions found in similar research can be implemented as well since the overall simulation model is not very sensitive to the exact value of these time constants.

3.7. Model combinations

With the model framework developed and the different components implemented in the simulation environment MATLAB Simulink *R2023b*, engine simulations could be executed using a combination of different compressor and turbine prediction methods. All remaining model parameters are presented in Table A2, Appendix 1. For the following validation and case study, the following combinations were investigated:

- 1 control volume with simplified turbocharger (1CV-simpleTC).
- 1 control volume with full turbocharger, compressor map predicted with Casey & Robinson, turbine map predicted with Jensen (1CV-CasJen).

Table 6. Parameters and settings for the implemented engine speed and fuel flow control.

Controller settings	Value	Actuator Parameters	Value
		Engine Speed Controller	
Proportional gain K_P	4.5	Quadratic coefficient discharge coefficient a_{C_D}	0.000 061 11 $^{\circ -2}$
Integral gain K_I	1.1	Linear coefficient discharge coefficient b_{C_D}	−0.0025 $^{\circ -1}$
Derivative gain K_D	0	Constant coefficient discharge coefficient c_{C_D}	0.72
		Throttle plate angle of closed throttle ψ_0	0°
		Throttle shaft to throttle bore ratio a	0.0909
		Time constant throttle valve τ_{THR}	0.05 s
		Fuel Flow Controller	
		Time constant fuel valve τ_{fuel}	0.1 s

- 1 control volume with full turbocharger, compressor map predicted with Stapersma, turbine map predicted with Stapersma (1CV-StaSta).
- 3 control volumes with full turbocharger, compressor map predicted with Stapersma, turbine map predicted with Stapersma (3CV-StaSta)
- 3 control volumes with full turbocharger, compressor map predicted with Stapersma, turbine map predicted with Jensen (3CV-StaJen)

4. Model validation

On the engine testbed of the NLDA, an engine transient measurement run of 5 consecutive load steps with intermediate steady state operation has been captured. The measurement run has been executed on constant engine speed with load steps increasing from 16% to 30%, 60%, and 80% and decreasing from 80% to 50% and 20% of the MCR load. These measurement points have been selected to cover the entire engine envelope, including increasing and decreasing step loads with different step sizes. This measurement campaign can be executed in a single run of less than 2 hours and should be integrated into future FAT of internal combustion engines. The obtained dataset has been split into two separate datasets, one set containing segments with steady state operating points and one set containing data of the dynamic segments with the transition between steady state operating points, see Figure 15. The steady state operating points have been used to calibrate the derived models while the dynamic segments have been used to validate the calibrated models. To determine the error between the measurements and the simulation results, three different indexes of performance (Ghelardoni et al. 2013; Coraddu et al. 2022) have been evaluated for the complete measurement run, all steady state segments and all dynamic segments. These indices are defined as follows:

(1) The mean absolute error (MAE):

$$\mathrm{MAE} = \frac{1}{m}\sum_{i=1}^{m}\left[h(x_i^t) - y_i^t\right], \tag{62}$$

with m the sample size, $h(x_i^t)$ the predicted model outcome for any given variable and for every sample point, and y_i^t the measurement of the given variable;

(2) The Mean Absolute Percentage Error (MAPE):

$$\mathrm{MAPE} = \frac{100}{m}\sum_{i=1}^{m}\left[\frac{h(x_i^t) - y_i^t}{y_i^t}\right]; \tag{63}$$

(3) The Pearson Product-Moment Correlation Coefficient (PPMCC):

$$\mathrm{PPMCC} = \frac{\sum_{i=1}^{m}(y_i^t - \bar{y})(h(x_i^t) - \hat{\bar{y}})}{\sqrt{\sum_{i=1}^{m}(y_i^t - \bar{y})^2}\sqrt{\sum_{i=1}^{m}(h(x_i^t) - \hat{\bar{y}})^2}}, \tag{64}$$

with $\bar{y} = \frac{1}{m}\sum_{i=1}^{m} y_i^t$ and $\hat{\bar{y}} = \frac{1}{m}\sum_{i=1}^{m} h(x_i^t)$.

The simulation was executed using the Runge-Kutta method and a fixed step-size of $0.0001s$. This increased the computational costs significantly, with an execution time of 240 s for a 300 s scenario, but the fixed step size ensured the correct ratio of sample points taken during the steady state and dynamic segments. For optimal performance, the simulation can be executed using a solver with variable step size, which will increase the step size during steady state segments, reducing the execution time to 6 s with the Dormand-Prince method and a maximum step size of 0.5 s. The simulation results have been obtained with MATLAB Simulink *R2023b* running on an Intel Core *i7−1365u* processor and 16 GB RAM.

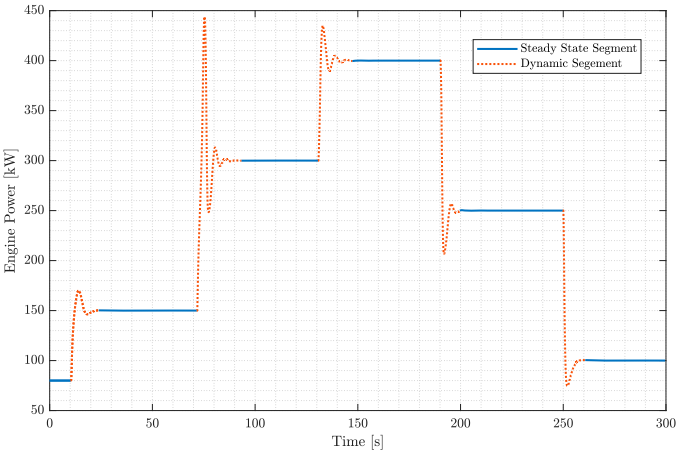

Figure 15. Engine power time trace showing the steady state and dynamic segments.

The complete set of results for all three performance indices and all model combinations is provided in Appendix 3. Tables 7 and 8 summarise the mean absolute percentage error (MAPE) of key variables for the calibration and validation datasets, respectively. Table 7 reports the MAPE for steady-state operating segments that coincide with the five calibration points. These values demonstrate that all model variants are well calibrated, with most engine variables predicted to within approximately 5% error (i.e. > 95% accuracy). Table 8 presents the corresponding MAPE for dynamic segments used for validation, capturing the model's predictive capability during transient operation outside the calibration range. As expected, the errors in Table 8 are generally higher than those in Table 7, reflecting the greater challenge of predicting fast transient responses and the combined influence of model and measurement uncertainties. The following sections provide a variable-by-variable discussion of the main sources of deviation and their physical causes.

The complete set of performance indices is provided in Appendix 3. Overall, most models reproduce the transient performance characteristics well, as reflected by high Pearson product–moment correlation coefficients (PPMCC), typically exceeding 0.9 for the evaluated engine parameters. Notable exceptions are the mass flow rates $\dot{m}_{in}$ and engine efficiency η_{eng}, both of which show lower correlations due to sensor response delays. With a sensor response delays of 3 second for air flow (Sierra Instruments [date unknown]) and 0.5 second for fuel flow (Bronkhorst [date unknown])), both sensors are slower than the engine's transient response. As a result, transient measurements of these variables, and therefore the derived efficiency, see Equation (8), are considered unreliable.

During steady-state operation, however, the fuel mass flow $\dot{m}_{fuel}$ and corresponding engine efficiency are predicted with very high accuracy, reflecting the quality of the in-cylinder combustion model. As discussed in Section 3.3, calibration of the Seiliger parameters produced an accurate representation of the combustion process and the associated energy losses, see Figure 4. Although the PPMCC for engine efficiency remains lower during dynamic phases, the fuel-flow predictions show comparatively higher accuracy, consistent with the shorter delay of the fuel-flow sensor relative to the air-flow sensor. This is particularly evident during the increases in load, when the response to fuel flow is captured well, while the predictions during the decreases in load are less accurate (see Figure 17(c)). This

Table 7. Mean Absolute Percentage Error (MAPE) steady state segments (Calibration Points).

Variable	1CV-SimpleTC	1CV-CasJen	1CV-StaSta	3CV-StaSta	3CV-StaJen
Engine Power P_b	0.67%	0.64%	0.66%	0.64%	0.67%
Engine Speed n_{eng}	0.06%	0.05%	0.07%	0.05%	0.08%
Throttle valve set point THR_{set}	6.48%	6.28%	4.49%	3.67%	5.71%
Turbocharger Speed n_{TC}	100.00%	3.76%	10.39%	4.72%	6.60%
Pressure air cooler p_{ac}	2.85%	1.60%	1.77%	1.14%	0.88%
Pressure inlet receiver p_{ir}	5.19%	5.20%	5.21%	1.79%	3.83%
Pressure outlet receiver p_{or}	1.68%	1.67%	1.68%	2.18%	4.24%
Total engine efficiency η_{eng}	2.04%	2.04%	2.06%	1.47%	1.48%
Mass flow air + fuel in $\dot{m}_{in}$	3.25%	3.24%	3.23%	2.64%	2.67%
Mass flow fuel $\dot{m}_{fuel}$	1.88%	1.72%	1.73%	1.35%	1.36%

Table 8. Mean Absolute Percentage Error (MAPE) dynamic segments (Validation).

Variable	1CV-SimpleTC	1CV-CasJen	1CV-StaSta	3CV-StaSta	3CV-StaJen
Engine Power P_b	7.20%	6.40%	5.52%	6.70%	5.29%
Engine Speed n_{eng}	0.61%	0.91%	0.64%	0.72%	0.97%
Throttle valve set point THR_{set}	30.47%	30.05%	30.96%	30.96%	27.37%
Turbocharger Speed n_{TC}	100.00%	5.54%	10.12%	8.34%	9.07%
Pressure air cooler p_{ac}	4.26%	3.15%	2.86%	5.12%	3.79%
Pressure inlet receiver p_{ir}	6.61%	6.42%	6.52%	5.16%	4.90%
Pressure outlet receiver p_{or}	3.70%	3.39%	2.20%	3.61%	4.79%
Total engine efficiency η_{eng}	6.79%	6.35%	6.37%	6.41%	5.93%
Mass flow air + fuel in $\dot{m}_{in}$	12.88%	12.72%	11.41%	11.40%	11.95%
Mass flow fuel $\dot{m}_{fuel}$	3.70%	4.22%	3.01%	3.73%	3.39%

highlights the influence of the pressure of the inlet receiver on the characteristic of the transient response.

During steady-state segments, PPMCC reaches 1 for all parameters and models, except engine speed and throttle position. Throttle oscillations–caused by sensor noise and external disturbances–lead to minor speed fluctuations, reducing correlation with static simulation outputs for the engine speed, see also Figure 16. However, throttle valve measurements still show high PPMCC (0.97), likely due to the variation in throttle positions. At high engine loads, throttle predictions deviate by 5-10% from measured values, suggesting minor errors in the discharge coefficient. While throttle actuation is accurately predicted at low loads, deviations increase at high loads due to the model's fixed PID gains, unlike the variable-gain controller in actual operation.

Pressures in the exhaust receiver p_{er} and before the throttle valve in the air cooler p_{ac} are predicted with $> 95\%$ accuracy at steady-state by all models. The inlet receiver pressure p_{ir} is best captured by the 3-control-volume (3CV) models. Transient pressure prediction remains above 93% for all models, with 3CV models outperforming simpler approaches. The simple turbocharger model shows the most significant drop in accuracy during transients, but performs better than expected. At high loads, all models–except 3CV-StaSta–underpredict p_{ir}, while 3CV-StaSta slightly underpredicts p_{er}, suggesting an overestimated turbocharger efficiency, see Figure 16(d).

The turbocharger shaft speed is predicted accurately during increasing load steps by all models with a full turbocharger implemented, see Figure 16(c). As expected from the compressor fitting, the models with a compressor prediction according to Stapersma show a larger deviation for the lower compressor speeds. Predictions of the turbocharger shaft speed during decreasing load steps are less accurate, which also affects the pressure predictions. The error of predicted p_{ac}, p_{ir} and p_{er} is larger during decreasing load steps compared to the increasing load steps, see also Figures 16(d) and 17(b). The worst deviation is achieved with the simple turbocharger model. Since this model captures the rotational inertia with a constant turbocharger time constant τ_{TC}, see Equation (28), the delay in the compressor outlet pressure is identical during increasing and decreasing load steps. The measurements show, however, that the turbocharger shaft speed is decreasing notably faster during decreasing load steps due to the drop in delivered turbine torque. This results in a significant over-prediction of p_{ac} and p_{ir}. A constant turbocharger time constant τ_{TC} is not suited to capture the transient performance characteristics of increasing and decreasing engine loads.

Only the 3CV models capture the pressure dynamics in the air cooler p_{ac} due to throttle valve action. Abrupt throttle openings at rising loads cause flow surges and pressure drops; closures during decreasing loads cause pressure spikes. Models without air cooler volume elements fail to reproduce this. While these effects minimally impact accuracy, they may influence compressor performance. A sudden pressure increase with a simultaneous drop in delivered mass flow could push the compressor across the surge line, as investigated and extensively discussed in Theotokatos and Kyrtatos (2003).

Temperature predictions are not validated for dynamic behaviour due to sensor delays. Validation in the steady state calibration points shows a $> 95\%$ accuracy.

The predicted temperatures for different locations in the engine have not been validated. Predicted temperatures in the steady state calibration points have been compared with the measured temperatures, and an error of less than 5% was achieved. However, it was not possible to validate the dynamic response characteristics due to the considerable sensor delay of the implemented temperature sensors. The current models do not account for heat losses to oil, ducting, or turbocharger components, excluding the air cooler, which may lead to overestimating gas path temperatures during rising loads. At the same time, measured values may under-represent actual temperatures.

The robustness of the Seiliger-cycle calibration across five operating points, and of the subsequent polynomial fitting, was evaluated using a leave-one-out procedure. In each iteration, the Seiliger parameters a, b, c, together with the mechanical efficiency η_m and heat release efficiency η_q, were re-calibrated while omitting one of the five operating points. The model was then re-validated and the performance indices were recomputed. This procedure was carried out four times for the 3CV-StaSta configuration, excluding the 20%, 60%, 80%, and 100% load points. The 50 percent point was not excluded because it closely resembles the 60 percent operating point. The resulting Mean Absolute Percentage Errors (MAPE) were compared

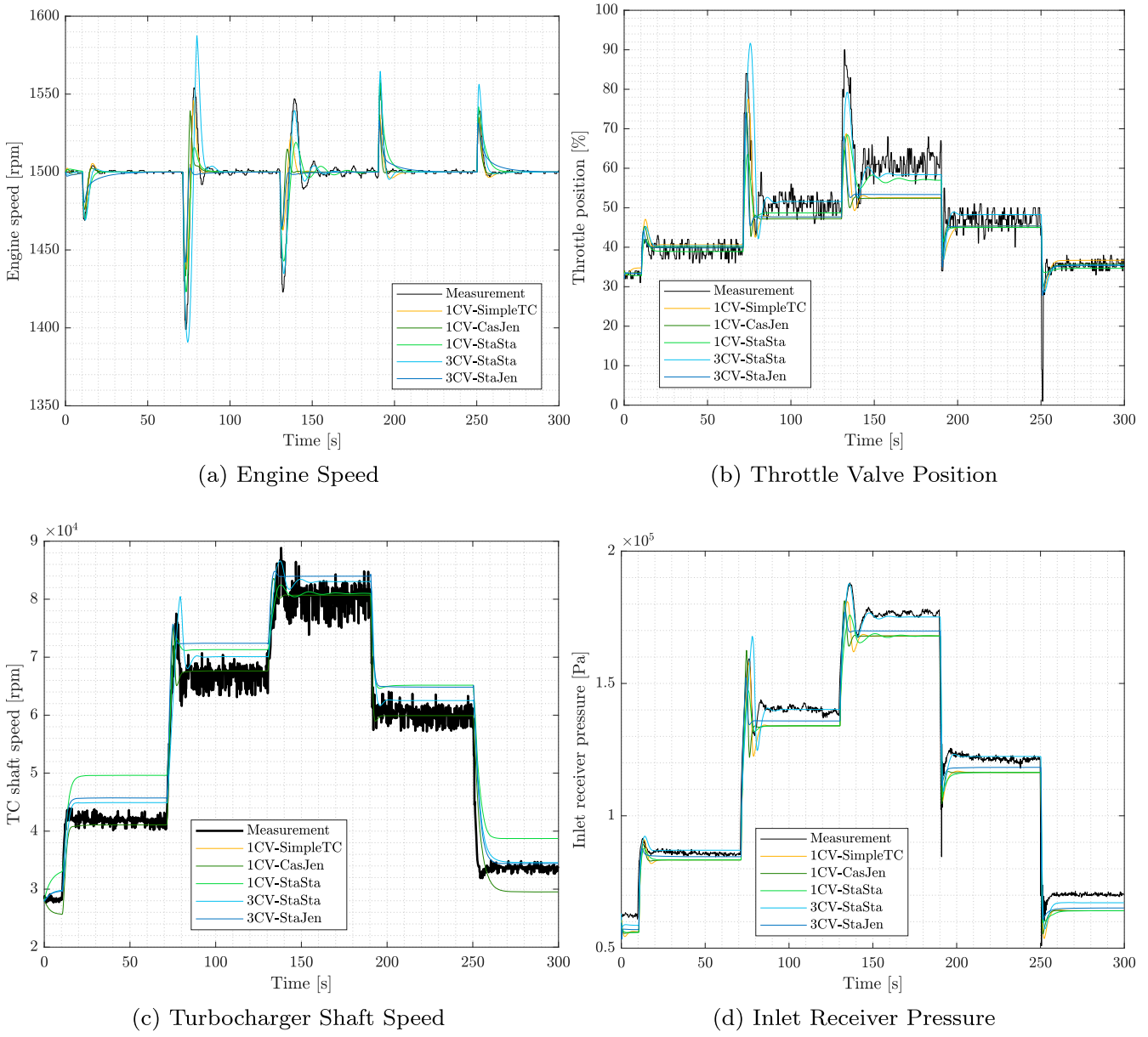

(a) Engine Speed

(b) Throttle Valve Position

(c) Turbocharger Shaft Speed

(d) Inlet Receiver Pressure

Figure 16. Validation time trace plots of engine speed, throttle valve position, turbocharger shaft speed and inlet receiver pressure. (a) Engine Speed. (b) Throttle Valve Position. (c) Turbocharger Shaft Speed and (d) Inlet Receiver Pressure.

with the reference calibration based on all five points, and the outcomes are provided in Appendix 4. As expected, omitting the 20% load point leads to the largest degradation in accuracy. However, for most parameters the deterioration remains minor, with the largest deviation found for the inlet receiver pressure at 2.67 percentage points. The effect of removing a calibration point at medium load is almost negligible. Overall, the leave-one-out analysis demonstrates that the chosen calibration and fitting approach is robust and remains reliable even when fewer calibration points are available.

5. Case study

With the derived simulation models, a series of 6 load steps have been investigated, see Table 9, and Figure 18(b). For these load steps, the limits provided within NATO (2021) on the quality of power supply were used as a guideline. Following a load change on the electric grid, the grid's frequency is allowed to deviate 4% from the steady state frequency of 60 Hz. This is defined as the transient tolerance, see Table 10. Under worst-case conditions, an excursion of 5.5% is permitted. For this use case, the grid is supposed to be fed from a single generator set. Because the simulation represents a single generator, a speed drop functionality was not included in the model. In addition, the mechanical coupling between the generator and the engine was assumed to be rigid, and shaft elasticity was therefore neglected. Therefore, the grid frequency is directly coupled to the engine speed, and the limits of STANAG 1008 can be applied to the engine speed as well. For the first load step, the engine load was increased from 200 kW to 305 kW, resulting in an engine speed drop of 3.8%, thus meeting the STANAG 1008 requirement for transient tolerances. For the second load step, the engine load was decreased to 200 kW. A load increase from 200 kW to 330 kW was investigated in load step 3, resulting in an engine speed drop of 5.2%, thus passing the STANAG 1008 requirement for worst case excursions. The corresponding load decrease from 330 kW to 200 kW was investigated in load step 4. For load steps 5 and 6, the load step was further increased from 200 kW to 350 kW and 380 kW. In both cases, solely the increasing

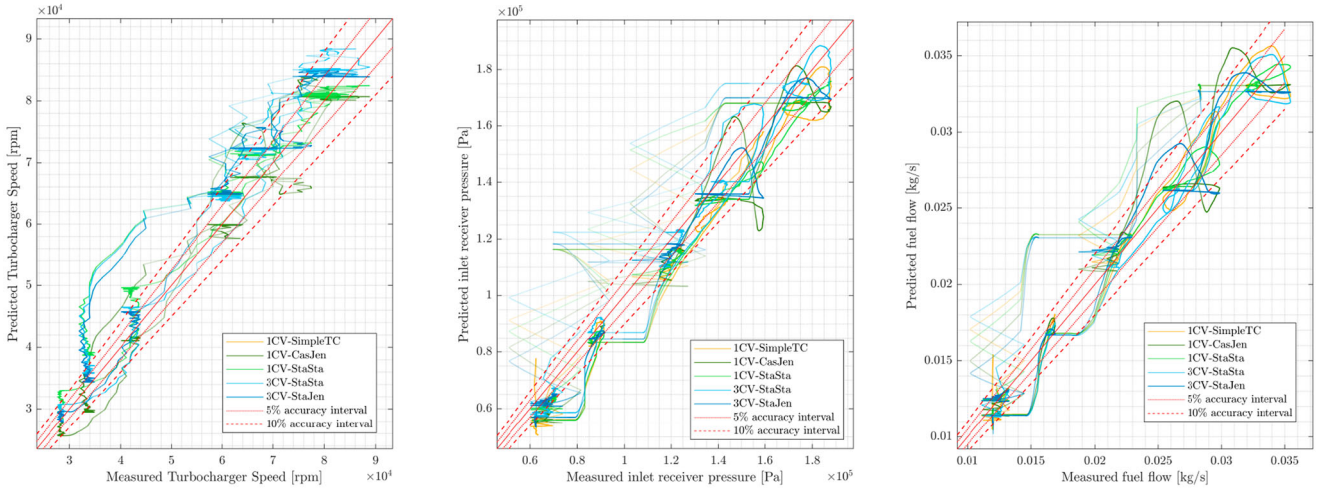

(a) Turbocharger Shaft Speed (b) Inlet Receiver Pressure (c) Fuel Flow

Figure 17. Validation scatter plots of turbocharger shaft speed, inlet receiver pressure and fuel flow with 5% and 10% accuracy interval lines, the colour intensity equals the frequency of occurrence. (a) Turbocharger Shaft Speed. (b) Inlet Receiver Pressure and (c) Fuel Flow.

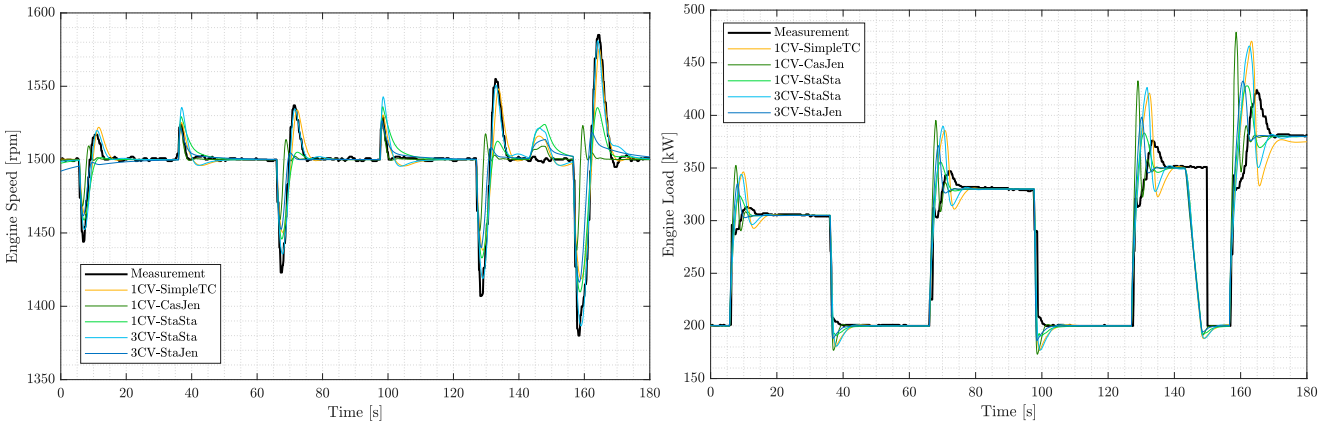

(a) Engine Speed (b) Engine Power

Figure 18. Measurement and simulation results for engine speed and engine power, showing over-shoot and settling due to the increasing and decreasing load steps. The load decrease at timestep 143 s was not measured and simulated with a decreasing ramp. (a) Engine Speed and (b) Engine Power.

step was recorded and investigated. Load step 6 represents the highest achievable load increase without stalling the engine, according to the simulation models with full turbocharger. An even higher load increase was not tested on the engine testbed. The simulation model with a simplified turbocharger was not able to simulate this load step since the charge air pressure does not increase fast enough to facilitate recovering the engine speed and prevent an engine stall. Results for this model are therefore generated with a load increase to 375 kW. The resulting time traces for engine speed and engine power are presented in Figure 18.

The simulations were performed with the Runge Kutta method using a fixed step size of 0.001 s. The execution times for the different model configurations are presented in Table 11. Results obtained with the Dormand Prince solver, which uses a variable step size with a maximum step size of 0.5 s, are also included in the same table. When a variable step size is used, the step size increases during steady state segments, which reduces the execution time for all model configurations. The effect of model complexity is reflected in the execution times as well. Increasing the number of differential equations from two in the simple turbocharger model to five in the three–control volume configurations results in a 40–70% increase in execution time. This trend appears consistently across both solver settings .

The results indicate that all models effectively capture the dynamic behaviour of engine speed; however, notable differences exist in recovery rates and settling times across the models. Generally, all models under-predict the speed drop during load increases and underestimate the overshoot during load decreases–except those utilising the Jensen-based turbine prediction. As expected from the validation, the 3CV-StaSta model provides the most accurate engine speed prediction, including recovery and settling characteristics during load increases. However, during load decreases, this model exhibits the largest over-prediction, slowest recovery, and longest settling time. Interestingly, the simpler 1CV-CasJen model with compressor prediction according to Casey & Robinson delivers the most accurate engine speed prediction during load decreases. Given the similarity in system response between Load Steps 1 & 2 and Load Steps 3 & 4, only the first two are analysed in detail. Likewise, due to comparable dynamics in Load Steps 5 & 6, only the final step is discussed in depth.

5.1. Load step 1 & 2: complying with stanag 1008

Load step 1 represents the maximum allowable load increase while complying with the NATO Stanag 1008 Transient Tolerance.

Table 9. Load Steps with measurement and simulation results of the engine speed deviation.

	Timestep	Initial Load	Target Load	Deviated Speed	Deviation
Step 1	5.7 s	200 kW	305 kW	1444 rpm	3.7%
Step 2	36.0 s	305 kW	200 kW	1525 rpm	1.6%
Step 3	66.0 s	200 kW	330 kW	1423 rpm	5.1%
Step 4	97.6 s	330 kW	200 kW	1529 rpm	1.9%
Step 5	127.0 s	200 kW	350 kW	1407 rpm	6.2%
Step 6	156.6 s	200 kW	280 kW	1380 rpm	8.0%
	1CV-SimpleTC	**1CV-CasJen**	**1CV-StaSta**	**3CV-StaSta**	**3CV-StaJen**
Step 1	1463 rpm (-1.31%)	1468 rpm (-1.66%)	1458 rpm (-0.97%)	1452 rpm (-0.55%)	1462 rpm (-1.27%)
Step 2	1525 rpm (0.07%)	1523 rpm (0.0%)	1529 rpm (0.34%)	1535 rpm (0.79%)	1522 rpm (-0.07%)
Step 3	1450 rpm (-1.89%)	1459 rpm (-2.53%)	1446 rpm (-1.62%)	1436 rpm (-0.91%)	1452 rpm (-2.04%)
Step 4	1530 rpm (0.07%)	1528 rpm (-0.07%)	1536 rpm (0.46%)	1543 rpm (0.92%)	1526 rpm (-0.20%)
Step 5	1438 rpm (-2.20%)	1451 rpm (-3.12%)	1433 rpm (-1.85%)	1419 rpm (-0.85%)	1440 rpm (-2.35%)
Step 6	1419 rpm (-2.82%)	1438 rpm (-4.20%)	1410 rpm (-2.17%)	1387 rpm (-0.51%)	1416 rpm (-2.61%)

Note: The error for the simulation is given in brackets, with a positive value indicating an over-prediction and a negative value indicating an under-prediction.

Table 10. QPS Frequency characteristics according to NATO (2021).

Characteristics	Tolerance	Transient Tolerance	Worst Case Excursion
Frequency 60 Hz	±3%	±4%	±5.5%
Recovery time	–	2 s	2 s

Accurate prediction of this step is critical for system sizing, layout of the power generation plant, and selecting switching behaviours of connected consumers Load Step 2 reflects the disconnection of major loads. The results for the relevant engine parameters are presented in Figure A19, Appendix 5. Models with more control volumes generally better capture the trends of the dynamic response characteristics, though not always with the highest pointwise accuracy. Key observations include:

Engine Speed: All models under-predict the speed drop during load increases and fail to fully capture overshoot and settling behaviour. Most recover too quickly, except for the 3CV-StaSta and 1CV-SimpleTC models. These two align more closely with measurements during the increase but respond too slowly during load decreases.

Throttle Valve Position: Throttle actuation is under-predicted across all models. During load increase, 3CV-StaJen most accurately captures the actuation profile. The 3CV-StaSta and 1CV-SimpleTC models predict the actuation height reasonably but lag in timing. Remaining models underestimate the actuation magnitude. For load decreases, all models significantly under-predict valve closure (predicted: 36%; measured: 20%).

Turbocharger Speed: Only the 1CV-StaJen model avoids steady-state errors. Models using Jensen's turbine prediction (1CV-CasJen and 3CV-StaJen) settle faster than measured during load increases but more accurately capture speed drops during load decreases. The 3CV-StaSta model best represents shaft dynamics during increases, but deviates most during decreases. This could be caused by the predicted compressor map and/or the turbine map deviating from the actual map for the area above the engine's steady state operating line.

Pressure Prediction: During load increases, the 3CV-StaSta model achieves the highest pressure prediction accuracy for air cooler, inlet, and exhaust receivers. However, it underperforms during load decreases, requiring more time to stabilise. Jensen-based turbine models over-predict pressure rise during increases but better capture dynamics during decreases than models using Stapersma's approach. The simplified turbocharger model (1CV-SimpleTC) shows substantial inaccuracies, particularly for compressor outlet p_{ac} and turbine inlet p_{er}, missing the transient dips and spikes caused by rapid throttle movements–effects well captured by 3CV models.

Air-Excess Ratio: This was not measured and thus cannot be validated, but simulated behaviour aligns with expectations, see Figure A19(f). During load increases, throttle opening boosts inlet receiver pressure and air mass flow before fuel flow catches up, temporarily spiking the air-excess ratio. All models replicate this transient lean phase, which is consistent with the implemented control logic. This behaviour contrasts with the control strategy of traditional diesel engines, where an increasing fuel flow counteracts a drop in engine speed, resulting in a drop in air-excess ratio. During load decreases, the throttle closes faster than the fuel valve, briefly enriching the mixture. This behaviour is also reflected across all models, though the dip magnitude varies. The air-excess ratio is generally more range-bound than diesel engines, which was expected to prevent knocking and misfires.

Temperature Prediction: Due to the significant temperature measurement lag of the implemented temperature sensors, only the measured steady state temperature is shown in Figure A19(g). At the 200 kW load point, the 3CV-StaSta model accurately predicts blowdown and exhaust receiver temperatures. At the 350 kW load point, it slightly overestimates blowdown temperature, while other models under-predict. Transient temperature changes are modest, as expected from the range-bound air-excess ratio, and no excessive thermal loading is anticipated.

5.2. Load step 6: largest possible load step

Load Step 6 represents the maximum load increase tolerable by the engine without stalling, as determined by simulations using full turbocharger models. Accurate prediction of this step is crucial, as it defines the system's ultimate dynamic capability prior to blackout conditions. The results for the relevant engine parameters are presented in Figure A20, Appendix 6. Compared to the results of load steps 1 and 2 in Figure A19, Appendix 5, model discrepancies are more pronounced. As expected, the 3CV-StaSta model best captures the trends across all key variables, particularly in recovery and settling behaviour. Notably, the model with a simplified turbocharger performs better than in previous steps, accurately capturing throttle position and pressure dynamics in the inlet and exhaust receivers. However, it shows significant distortions in air-excess ratio, blowdown temperature, and exhaust receiver temperature due to nonlinear effects. The 1CV-CasJen model performs the poorest, consistently under-predicting all investigated parameters. Its turbocharger speed and pressure responses are overly aggressive, indicating mismatched time delays of the valves and rotational inertia for turbocharger and engine speed within the model for this load step.

Table 11. Execution times for the different models and a simulation time of 180 s.

Execution Time	1CV-SimpleTC	1CV-CasJen	1CV-StaSta	3CV-StaSta	3CV-StaJen
Runge-Kutta solver, fixed timestep 0.001 s					
Run 1	12.21 s	14.24 s	14.73 s	16.79 s	20.35 s
Run 2	12.99 s	14.88 s	15.26 s	16.85 s	20.79 s
Real-time factor	13.8-14.8	12-12.6	≈ 12	≈ 10.7	≈ 8.7
Dormand-Prince solver, variable timestep, max timestep 0.5 s					
Run 3	1.95 s	3.53 s	3.11 s	3.35 s	3.12 s
Run 4	1.88 s	3.59 s	3.02 s	2.81 s	3.05 s
Real-time factor	≈ 95	≈ 50	≈ 55	≈ 55	≈ 55

6. Conclusions and future work

This study explored, compared, and validated several gas path modelling approaches for mean value first principle engine models (MVFPEM), focussing on the transient behaviour of the gas exchange process and turbocharger dynamics. These models aim to support dynamic system analysis, control design, and integration into Digital Twin or Hardware-in-the-Loop applications, where real-time capability is essential. The dynamic response of a high-speed, four-stroke spark-ignited gas engine was assessed using models calibrated with minimal data, primarily from project guidelines, manufacturer specifications, publicly available data, and factory acceptance test (FAT) measurements. A sequence of five load steps was used for validation, with an additional load step designed to meet NATO STANAG 1008 criteria to evaluate ultimate dynamic performance.

Key findings include:

(1) **Calibration with Minimal Data:** Dynamic MVFPEMs can be effectively calibrated using steady-state data; except for the values of the time delays τ_{TC}, τ_{THR} and τ_{fuel}, requiring one dedicated measurement of a load step. All engine parameters deemed relevant to analyse the dynamic response characteristics of a larger propulsion or power-generating system, or for control purposes, could be validated with a single transient measurement run. Integrating these transient measurement campaigns into the FAT process enhances the utility of standard FAT data for future model development and validation.

(2) **Turbocharger Map Prediction:** Performance maps can be estimated up to a certain degree of accuracy using limited steady-state data at constant speed. However, as all measurement points lie on the engine's steady-state line, the full turbocharger envelope cannot be validated. Results on the turbocharger speed during load steps suggest that the performance maps for compressor and turbine according to Stapersma resulted in a better fit during a load increase (below the engine's steady state operating line), while the methods of Casey and Jensen resulted in a better fit during a load decrease (above the turbocharger steady state operating line).

(3) **Model Accuracy:** All models achieved higher then 95% accuracy for key parameters for steady-state simulation. These key parameters included engine speed, turbocharger speed, throttle position and the pressures of the different gas path volumes. Dynamic accuracy decreased slightly across all models, with the 3CV models showing the least degradation. Larger errors were observed for mass flow and throttle actuation due to sensor delays and simplified PID implementation, which uses fixed gains, unlike the actual variable-gain controllers.

(4) **Simplified Turbocharger Model Limitations:** While a simplified turbocharger model (with the turbocharger power balance from Equation (26)) can yield accuracies of more than 90% for many parameters, it fails to capture the inertial effects during load decreases. The fixed turbocharger time constant cannot replicate the rapid deceleration observed in measurements, limiting this model's suitability for dynamic simulations involving load reversals.

(5) **Air-Excess Ratio and Temperature Trends:** Although not directly validated due to sensor delays, the predicted trends in air-excess ratio and temperatures are consistent with the expected behaviour. The implemented control strategy effectively moderates air-excess ratio fluctuations, helping prevent knock, misfire, and thermal overloading, though at the cost of limited dynamic performance and slower transient recovery.

(6) **Impact of Control Volume Reduction:** Reducing the amount of control volumes does not necessarily decrease the complexity of the model. Especially replacing the volume element of the exhaust receiver with a simple pressure and temperature loss results in an increased model complexity to predict the blowdown pressure and temperature.

Overall, to accurately predict dynamic response characteristics, MVFPEMs should include at least two control volumes (inlet and exhaust receivers) and ideally a third for the charge air cooler. A complete turbocharger model is also essential, even if the performance maps for the compressor and turbine are unavailable. In such cases, Stapersma's map prediction method is recommended due to its accuracy, minimum data requirements, and the possibility of generating turbine and compressor data with the same set of equations. The strengths and limitations of the different modelling approaches are summarised in Table 12.

Further efforts should also address controller fidelity. The simplified control strategies used here reproduce general dynamics well, but deviations at extreme load conditions may stem from controller approximations. However, incorporating more complex control models requires careful consideration, given limited access to OEM controller data and the need to generalise the MVFPEMs across engine platforms.

Finally, the presented modelling approaches provide a robust foundation for future research on the combustion of alternative fuels in marine internal combustion engines. The implemented in-cylinder combustion model can be adapted and recalibrated for a wide variety of fuels and different engine speeds, provided that p–V measurements are available. Once calibrated, the Seiliger cycle enables reliable prediction of peak pressure, fuel consumption, and exhaust pressure and temperature. These outputs are critical for assessing dynamic response characteristics and turbocharger operating points when engines operate on different fuels or during transitions between fuels. Such adaptability is particularly relevant as the maritime sector seeks compliance with increasingly stringent emission regulations and pursues decarbonisation strategies that require fuel flexibility. The methodology is not limited to the investigated case but can be generalised to other engine types and operating conditions, enhancing its value as a practical modelling framework.

At present, the framework can only predict CO_2 emissions, as these are directly linked to fuel consumption, while the prediction of other emissions is constrained by the use of mean-value

Table 12. Strengths and limitations of the different modelling approaches.

Model	Strengths	Limitations
1CV-SimpleTC	Low model complexity	No prediction of turbocharger speed
	No turbocharger maps required	Reduced accuracy and fidelity during transients
	Minimal calibration effort	Complex blowdown modelling
1CV-CasJen	Improved transient performance	Overprediction during load increases
	Good dynamic fidelity during load decreases	Poor compressor map accuracy at very low pressure ratios
	Compressor map requires only one design point	Complex blowdown modelling
1CV-StaSta	Improved transient prediction	Lower pressure fidelity during transients
	Consistent compressor and turbine map methodology	Turbine map calibration challenging with limited data
	Highest accuracy for turbocharger speed	Complex blowdown modelling
3CV-StaSta	Highest overall accuracy	High calibration effort
	Strong dynamic fidelity, particularly for load increases	Demanding initialisation, setting of initial conditions
	Consistent compressor and turbine map methodology	Turbine map calibration difficult with sparse data
		Slight overprediction of exhaust temperatures
3CV-StaJen	High overall accuracy	High calibration effort
	Strong dynamic fidelity, particularly for load decreases	Demanding initialisation, setting of initial conditions
		Slight underprediction of exhaust temperatures

representations of the in-cylinder process. Nevertheless, the current in-cylinder combustion-model could be replaced with more advanced combustion models to enable the prediction of NO_x, SO_x, and particulate matter *PM*, while maintaining the existing gas-path framework. Furthermore, the approach can be extended to dual-fuel CI engines by omitting the throttle valve and including an evaporation model, such as that proposed by Aquino (1981). Future research should therefore focus on validating the framework against experimental datasets for alternative fuels, integrating detailed emission sub-models, and coupling the results with ship energy system models. In doing so, the approach can support holistic assessments of alternative fuel pathways and their implications for vessel performance, efficiency, and regulatory compliance. Beyond fuel substitution alone, the framework will also be extended to variable-speed operation, which is particularly relevant for propulsion systems in which efficiency gains are closely linked to speed variability. This extension is equally important for the integration of emerging DC grid applications, in which engines operating on diesel or alternative fuels must provide both flexibility and resilience in increasingly complex marine energy systems.

Notes

1. GT-Power by Gamma Technologies: https://www.gtisoft.com/gt-suite-applications/gt-power/
2. Ricardo Wave by Ricardo Software: https://software.ricardo.com/products/ricardo-wave

Acknowledgments

The authors would like to thank the staff of the engine laboratory of the Netherlands Defence Academy for their support and assistance during the measurement campaign. The authors acknowledge the use of OpenAI's ChatGPT to support the refinement of writing style and language clarity. No AI-generated content was used for the development of ideas, analysis, or conclusions presented in this paper.

Disclosure statement

No potential conflict of interest was reported by the author(s).

Funding

This research is supported by the project MENENS, funded by the Netherlands Enterprise Agency (RVO) under the grant number MOB21012.

ORCID

Jasper Vollbrandt http://orcid.org/0009-0009-6816-1146

References

Acanfora M, Altosole M, Balsamo F, Micoli L, Campora U. 2022. Simulation modeling of a ship propulsion system in waves for control purposes. J Mar Sci Eng. 10(1):36. https://doi.org/10.3390/jmse10010036

Al-Busaidi W, Pilidis P. 2015. A new method for reliable performance prediction of multi-stage industrial centrifugal compressors based on stage stacking technique: Part ii–new integrated model verification. Appl Therm Eng. 90:927–936. https://doi.org/10.1016/j.applthermaleng.2015.07.081

Altosole M, Benvenuto G, Campora U, Laviola M, Zaccone R. 2017. Simulation and performance comparison between diesel and natural gas engines for marine applications. Proc Inst Mech Eng Pt M J Eng Marit Environ. 231(2):690–704.

Altosole M, Figari M. 2011. Effective simple methods for numerical modelling of marine engines in ship propulsion control systems design. J Nav Archit Mar Eng. 8(2):129–147. https://doi.org/10.3329/jname.v8i2.7366

Angulo-Brown F, Fernandez-Betanzos J, Diaz-Pico C. 1994. Compression ratio of an optimized air standard otto-cycle model. Eur J Phys. 15(1):38–42. https://doi.org/10.1088/0143-0807/15/1/007

Aquino CF. 1981. Transient a/f control characteristics of the 5 liter central fuel injection engine. SAE Trans. 90:1819–1833.

Arifin M, Kusnadi, Pramana RI. 2018. Prediction performance map of radial compressor for system simulation. In: 2018 International Conference on Sustainable Energy Engineering and Application (ICSEEA). IEEE. p. 51–56.

Baan G. 2025. Assessment of efficiency potential hybrid electric turbocharging si ice [master's thesis]. Delft University of Technology.

Baines NC. 2005. Fundamentals of turbocharging. Concepts NREC.

Baker R, Daby E. 1977. Engine mapping methodology. SAE Technical Paper.

Baldi F, Theotokatos G, Andersson K. 2015. Development of a combined mean value–zero dimensional model and application for a large marine four-stroke diesel engine simulation. Appl Energy. 154:402–415. https://doi.org/10.1016/j.apenergy.2015.05.024

Benson I. 1983. Thermodynamics and gas dynamics of internal combustion engines. J Fluid Mech. 134:45S469.

Benson RS, Ledger J, Whitehouse ND, Walmsley S. 1973. Comparison of experimental and simulated transient responses of a turbocharged diesel engine. SAE Trans. 82:2424–2447.

Benvenuto G, Campora U. 2002. Dynamic simulation of a high-performance sequentially turbocharged marine diesel engine. Int J Engine Res. 3(3):115–125. https://doi.org/10.1243/14680870260189244

Blumberg PN. 1976. Powertrain simulation: A tool for the design and evaluation of engine control strategies in vehicles. SAE Technical Paper.

Bondarenko O, Fukuda T. 2020. Development of a diesel engine's digital twin for predicting propulsion system dynamics. Energy. 196:117126. https://doi.org/10.1016/j.energy.2020.117126

Boose B. 2014. 3d cfd simulation von turboladern innerhalb einer motorumgebung [dissertation]. Universität Stuttgart.

Bosklopper J et al. 2020. Experimental study on a retrofitted marine size spark-ignition engine running on port-injected 100% methanol. In: Conference proceedings of INEC. IMarEST.

Boyce MP. 2011. Gas turbine engineering handbook. Elsevier.

Bronkhorst. ([date unknown]). Datasheet f-106ci.

Brugård J, Eriksson L, Nielsen L. 2001. Mean value engine modeling of a turbo charged spark ignited engine: A principle study. Department of Electrical Engineering.

Caligiuri C, Renzi M. 2017. Combustion modelling of a dual fuel diesel–producer gas compression ignition engine. Energy Procedia. 142:1395–1400. https://doi.org/10.1016/j.egypro.2017.12.525
Casey M, Robinson C. 2013. A method to estimate the performance map of a centrifugal compressor stage. J Turbomach. 135(2):021034. https://doi.org/10.1115/1.4006590
Casey M, Robinson C. 2023. Some properties of the exit velocity triangle of a radial compressor impeller. J Turbomach. 145(5):051007. https://doi.org/10.1115/1.4056088
Casey M, Rusch D. 2014. The matching of a vaned diffuser with a radial compressor impeller and its effect on the stage performance. J Turbomach. 136(12):121004. https://doi.org/10.1115/1.4028218
Casoli P et al. 2014. Development and validation of a 'crank-angle' model of an automotive turbocharged engine for hil applications. Energy Procedia. 45:839–848. https://doi.org/10.1016/j.egypro.2014.01.089
Cassidy JF. 1977. A computerized on-line approach to calculating optimum engine calibrations. SAE Trans. 86:293–308.
Chauvin J, Grondin O, Moulin P. 2011. Control oriented model of a variable geometry turbocharger in an engine with two egr loops. Oil Gas Sci Technol. 66(4):563–571. https://doi.org/10.2516/ogst/2011103
Chesse P, Chalet D, Tauzia X, Hetet J, Inozu B. 2004. Real-time performance simulation of marine diesel engines for the training of navy crews. Mar Technol SNAME News. 41(03):95–101. https://doi.org/10.5957/mt1.2004.41.3.95
Coraddu A et al. 2022. Physical, data-driven and hybrid approaches to model engine exhaust gas temperatures in operational conditions. Sh offshore Struct. 17(6):1360–1381. https://doi.org/10.1080/17445302.2021.1920095
Coraddu A, Kalikatzarakis M, Theotokatos G, Geertsma R, Oneto L. 2021. Physical and data-driven models hybridisation for modelling the dynamic state of a four-stroke marine diesel engine. In: Engine modeling and simulation. Springer. p 145–193.
Costall A. 2007. A one-dimensional study of unsteady wave propagation in turbocharger turbines [dissertation]. Imperial College London.
Curto-Risso PL, Medina A, Hernández AC. 2008. Theoretical and simulated models for an irreversible otto cycle. J Appl Phys. 104(9):094911. https://doi.org/10.1063/1.2986214
Ding Y, Sui C, Li J. 2018. An experimental investigation into combustion fitting in a direct injection marine diesel engine. Appl Sci. 8(12):2489. https://doi.org/10.3390/app8122489
El Hadef J. 2014. Approche quasi-systématique du contrôle de la chaîne d'air des moteurs suralimentés, basée sur la commande prédictive non linéaire explicite [dissertation]. Université d'Orléans.
El Hameur MA, Cerdoun M, Tarabet L. 2024. An improved model for primary prediction of performance map for turbocharger radial turbine. Mech Eng Pt D J Automobile Eng. 239.
Eriksson L et al. 2002. Modeling of a turbocharged si engine. Annu Rev Control. 26(1):129–137. https://doi.org/10.1016/S1367-5788(02)80022-0
Eriksson L, Andersson I. 2002. An analytic model for cylinder pressure in a four stroke si engine. SAE Trans. 111:726–733.
Fatsis A, Vlachakis N, Leontis G. 2021. A centrifugal compressor performance map empirical prediction method for automotive turbochargers. Int J Turbo Jet Engine. 38(4):411–420. https://doi.org/10.1515/tjj-2019-0006
Galindo J et al. 2016. Compressor efficiency extrapolation for 0d-1d engine simulations. SAE Technical Paper.
Galindo J, Luján J, Climent H, Guardiola C. 2007. Turbocharging system design of a sequentially turbocharged diesel engine by means of a wave action model. SAE Trans. 116:1045–1056.
Gašparović N, Stapersma D. 1973. Berechnung der kennfelder mehrstufiger axialer turbomaschinen. Forsch Ingenieurwes A. 39(5):133–143. https://doi.org/10.1007/BF02560482
Geertsma R, Negenborn R, Visser K, Loonstijn M, Hopman J. 2017. Pitch control for ships with diesel mechanical and hybrid propulsion: modelling, validation and performance quantification. Appl Energy. 206:1609–1631. https://doi.org/10.1016/j.apenergy.2017.09.103
Georgescu I, Stapersma D, Nerheim LM, Mestemaker B. 2016. Characterisation of large gas and dual-fuel engines. MTZ Ind. 6(3):64–71. https://doi.org/10.1007/s40353-016-0029-z
Ghaemi MH, Zeraatgar H. 2021. Analysis of hull, propeller and engine interactions in regular waves by a combination of experiment and simulation. J Mar Sci Technol. 26(1):257–272. https://doi.org/10.1007/s00773-020-00734-5
Ghelardoni L, Ghio A, Anguita D. 2013. Energy load forecasting using empirical mode decomposition and support vector regression. IEEE Trans Smart Grid. 4(1):549–556. https://doi.org/10.1109/TSG.5165411
Guan C, Theotokatos G, Chen H. 2015. Analysis of two stroke marine diesel engine operation including turbocharger cut-out by using a zero-dimensional model. Energies. 8(6):5738–5764. https://doi.org/10.3390/en8065738
Guzzella L, Onder C. 2009. Introduction to modeling and control of internal combustion engine systems. Springer Science & Business Media.
Hendricks E. 1989. Mean value modelling of large turbocharged two-stroke diesel engines. SAE Trans. 98:986–998.
Hendricks E. 1997. Engine modelling for control applications: a critical survey. Meccanica. 32(5):387–396. https://doi.org/10.1023/A:1004247514972
Heywood JB. 1988. Internal combustion engine fundamentals. Mcgraw-Hill.
Hoang AT et al. 2022. Energy-related approach for reduction of co2 emissions: A critical strategy on the port-to-ship pathway. J Clean Prod355:131772. https://doi.org/10.1016/j.jclepro.2022.131772
Horlock JH, Winterbone D. 1986. The thermodynamics and gas dynamics of internal-combustion engines. Vol. II. Oxford University Press.
Hubbard M. 1975. Applications of automatic control to internal combustion engines [dissertation]. Stanford University.
Inal OB, Charpentier JF, Deniz C. 2022. Hybrid power and propulsion systems for ships: current status and future challenges. Renew Sustain Energy Rev. 156:111965. https://doi.org/10.1016/j.rser.2021.111965
Jensen JP, Kristensen A, Sorenson SC, Houbak N, Hendricks E. 1991. Mean value modeling of a small turbocharged diesel engine. SAE Technical Paper.
Kiouranakis KI, Vos Pd, Willems R, Sapra HD, Geertsma R. 2025. Dual-phase combustion behavior in a converted marine natural gas si engine: exploring the impact of bowl-in and squish phases on performance and emissions. Appl Therm Eng. 269:1–26.
Kolmanovsky I, Moraal P, Van Nieuwstadt M, Stefanopoulou A. 2022. Issues in modelling and control of intake flow in variable geometry turbocharged engines. In: Systems Modelling and Optimization Proceedings of the 18th IFIP TC7 Conference. Routledge. p 436–445.
Kumar S, Chauhan MK, Varun. 2013. Numerical modeling of compression ignition engine: A review. Renew Sustain Energy Rev. 19:517–530. https://doi.org/10.1016/j.rser.2012.11.043
Ledger J, Benson R, Whitehouse N. 1971. Dynamic modeling of a turbocharged diesel engine. SAE Transactions, paper (710177). p 1–12.
Ledger J, Walmsley S. 1971. Computer simulation of a turbocharged diesel engine operating under transient load conditions. SAE Technical Paper.
Mai H, Bolz H. 2015. Validierung von turboladerkennfeldern auf heißgasprüfständen. ATZextra. 20(8):54–59. https://doi.org/10.1007/s35778-015-0042-9
Maroteaux F, Saad C. 2015. Combined mean value engine model and crank angle resolved in-cylinder modeling with nox emissions model for real-time diesel engine simulations at high engine speed. Energy. 88:515–527. https://doi.org/10.1016/j.energy.2015.05.072
Maroteaux F, Saad C, Aubertin F. 2015. Development and validation of double and single wiebe function for multi-injection mode diesel engine combustion modelling for hardware-in-the-loop applications. Energy Convers Manag. 105:630–641. https://doi.org/10.1016/j.enconman.2015.08.024
McKinlay CJ, Turnock SR, Hudson DA. 2021. Route to zero emission shipping: hydrogen, ammonia or methanol? Int J Hydrog Energy. 46(55):28282–28297. https://doi.org/10.1016/j.ijhydene.2021.06.066
Merker GP, Schwarz C, Stiesch G, Otto F. 2005. Simulating combustion: simulation of combustion and pollutant formation for engine-development. Springer Science & Business Media.
Mestemaker B, Castro MG, Den HeuvelVan H, Visser K. 2020. Dynamic simulation of a vessel drive system with dual fuel engines and energy storage. Energy. 194:116792. https://doi.org/10.1016/j.energy.2019.116792
Mizythras P, Boulougouris E, Theotokatos G. 2018. Numerical study of propulsion system performance during ship acceleration. Ocean Eng. 149:383–396. https://doi.org/10.1016/j.oceaneng.2017.12.010
Moraal P, Kolmanovsky I. 1999. Turbocharger modeling for automotive control applications. SAE Technical Paper.
NATO. 2021. Nato – stanag 1008: Characteristics of shipboard 440v/230v/115v 60hz, 440v/115v 400hz and 24/28vdc electrical power systems in warships of the nato navies. North Atlantic Treaty Organization (NATO).
Nickel J, Grigoriadis P. 2008. Verfahren und messmethoden zur erfassung von turboladerkennfeldern an turboladerprüfständen. In: Simulation und aufladung von verbrennungsmotoren. Springer. p 195–210.
Oleksiy B, Masashi K. 2010. Dynamic behaviour of ship propulsion plant in actual seas. Marine Eng. 45(Special):1012–1016. https://doi.org/10.5988/jime.45.1012
Parnell P. 1970. The digital simulation of a diesel engine operating under transient load conditions [dissertation]. University of Manchester Institute of Science and Technology.
Payri F, Benajes J, Galindo J, Serrano J. 2002. Modelling of turbocharged diesel engines in transient operation. part 2: wave action models for calculating the transient operation in a high speed direct injection engine. Proc Inst Mech Eng D J Automob Eng. 216(6):479–493. https://doi.org/10.1243/09544070260137507
Payri F, Reyes E, Serrano J. 1999. A model for load transients of turbocharged diesel engines. SAE Trans. 108:363–375.
Powell JD. 1987. A review of ic engine models for control system design. IFAC Proc Vol. 20(5):235–240. https://doi.org/10.1016/S1474-6670(17)55378-1

Pucher H, Zinner K. 2012. Aufladung von verbrennungsmotoren: grundlagen, berechnungen, ausführungen. Springer-Verlag.
Rakopoulos C, Scott M, Kyritsis D, Giakoumis E. 2008. Availability analysis of hydrogen/natural gas blends combustion in internal combustion engines. Energy. 33(2):248–255. https://doi.org/10.1016/j.energy.2007.05.009
Rakopoulos CD, Giakoumis EG. 2006. Review of thermodynamic diesel engine simulations under transient operating conditions. SAE Trans. 115:467–504.
Rakopoulos CD, Giakoumis EG. 2009. Diesel engine transient operation. Springer.
Rakopoulos CD, Giakoumis EG, Michos CN. 2007. Quasi-linear versus filling and emptying modelling applied to the transient operation of a turbocharged diesel engine. Int J Veh Des. 45(1-2):150–170. https://doi.org/10.1504/IJVD.2007.013675
Raptotasios SI, Sakellaridis NF, Papagiannakis RG, Hountalas DT. 2015. Application of a multi-zone combustion model to investigate the nox reduction potential of two-stroke marine diesel engines using egr. Appl Energy. 157:814–823. https://doi.org/10.1016/j.apenergy.2014.12.041
Reß J, Stürzebecher C, Bohn C, Märzke F, Frase R. 2015. A diesel engine model including exhaust flap, intake throttle, lp-egr and vgt, part i: system modeling. IFAC-PapersOnLine. 48(15):52–59.
Rusman J. 2018. Charge air configurations for propulsion diesel engines aboard fast naval combatants. In: Conference Proceedings of INEC. IMarEST. p 1–11.
Sapra H et al. 2020. Hydrogen-natural gas combustion in a marine lean-burn si engine: A comparitive analysis of seiliger and double wiebe function-based zero–dimensional modelling. Energy Convers Manag. 207:112494. https://doi.org/10.1016/j.enconman.2020.112494
Sapra H, Linden Y, van Sluijs W, Godjevac M, Visser K. 2019. Experimental investigations of performance variations in marine hydrogen-natural gas engines. In: Cimac Congress. vol. 2019. CIMAC, p 1–17.
Saravanamuttoo HI, Rogers GFC, Cohen H. 2001. Gas turbine theory. Pearson education.
Scappin F, Stefansson SH, Haglind F, Andreasen A, Larsen U. 2012. Validation of a zero-dimensional model for prediction of nox and engine performance for electronically controlled marine two-stroke diesel engines. Appl Therm Eng. 37:344–352. https://doi.org/10.1016/j.applthermaleng.2011.11.047
Schulten P. 2005. The interaction between diesel engines, ship and propellers during manouevring [dissertation]. Delft University of Technology.
Schulten PJ, Stapersma D. 2003. Mean value modelling of the gas exchange of a 4-stroke diesel engine for use in powertrain applications. SAE Technical Paper.
Seiliger M. 1926. Die hochleistungs-dieselmotoren. J. Springer.
Sein MH, Bo SJ. 2020. Prediction of marine diesel engine combustion characteristic in transient condition by using seiliger process cycle. IOP Conf Ser Mater Sci Eng. 717(1):012016. https://doi.org/10.1088/1757-899X/717/1/012016
Sierra Instruments. ([date unknown]). Quadratherm 640i-780i. QTherm V3.
Stapersma D. 2010. Diesel engines – volume 2: turbocharging. Netherlands Defense Academy.
Stapersma D. 2019. A general model for off-design performance of a single stage turbomachine, issue e. Delft University of Technology.
Stockar S et al. 2013. Modeling wave action effects in internal combustion engine air path systems: comparison of numerical and system dynamics approaches. Int J Engine Res. 14(4):391–408. https://doi.org/10.1177/1468087412455747
Stoumpos S et al. 2018. Marine dual fuel engine modelling and parametric investigation of engine settings effect on performance-emissions trade-offs. Ocean Eng. 157:376–386. https://doi.org/10.1016/j.oceaneng.2018.03.059
Stoumpos S, Theotokatos G, Mavrelos C, Boulougouris E. 2020. Towards marine dual fuel engines digital twins–integrated modelling of thermodynamic processes and control system functions. J Mar Sci Eng. 8(3):200. https://doi.org/10.3390/jmse8030200
Sui C et al. 2022. Mean value first principle engine model for predicting dynamic behaviour of two-stroke marine diesel engine in various ship propulsion operations. Int J Nav Archit Ocean Eng. 14:100432. https://doi.org/10.1016/j.ijnaoe.2021.100432
Sui C, Song E, Stapersma D, Ding Y. 2017. Mean value modelling of diesel engine combustion based on parameterized finite stage cylinder process. Ocean Eng. 136:218–232. https://doi.org/10.1016/j.oceaneng.2017.03.029
Sun Y, Wang H, Yang C, Wang Y. 2017. Development and validation of a marine sequential turbocharging diesel engine combustion model based on double wiebe function and partial least squares method. Energy Convers Manag. 151:481–495. https://doi.org/10.1016/j.enconman.2017.08.085
Swain E. 2005. Improving a one-dimensional centrifugal compressor performance prediction method. Proc Inst Mech Eng A J Power Energy. 219(8):653–659.
Tadros M, Ventura M, Soares CG. 2019. Simulation of the performance of marine genset based on double-wiebe function. In: Sustainable development and innovations in marine technologies. CRC Press. p 292–299.
Tadros M, Vettor R, Ventura M, Guedes Soares C. 2022. Effect of propeller cup on the reduction of fuel consumption in realistic weather conditions. J Mar Sci Eng. 10(8):1039. https://doi.org/10.3390/jmse10081039
Theotokatos G. 2010. On the cycle mean value modelling of a large two-stroke marine diesel engine. Proc Inst Mech Eng Pt M J Eng Marit Environ. 224(3):193–205.
Theotokatos G, Guan C, Chen H, Lazakis I. 2018. Development of an extended mean value engine model for predicting the marine two-stroke engine operation at varying settings. Energy. 143:533–545. https://doi.org/10.1016/j.energy.2017.10.138
Theotokatos G, Kyrtatos N. 2003. Investigation of a large high-speed diesel engine transient behavior including compressor surging and emergency shutdown. J Eng Gas Turbines Power. 125(2):580–589. https://doi.org/10.1115/1.1559903
Van Basshuysen R, Schäfer F, Trans T. 2016. Internal combustion engine handbook. SAE International.
Van Spronsen P, Tousain R. 2001. An optimal control approach to preventing marine diesel engine overloading aboard karel doorman class frigates. IFAC Proc Vol. 34(7):493–498. https://doi.org/10.1016/S1474-6670(17)35130-3
Verhelst S, Sheppard C. 2009. Multi-zone thermodynamic modelling of spark-ignition engine combustion–an overview. Energy Convers Manag. 50(5):1326–1335. https://doi.org/10.1016/j.enconman.2009.01.002
Vollbrandt J, Coraddu A, Geertsma R. 2023. Transient performance of alternatively fueled internal combustion engines for naval applications. In: Conference Proceedings of EAAW. IMarEST, p 1–11.
Wahlström J, Eriksson L. 2010. Modeling of a diesel engine with intake throttle, vgt, and egr. Linköping University Electronic Press. p 1–58.
Wang H, Gan H, Theotokatos G. 2020. Parametric investigation of pre-injection on the combustion, knocking and emissions behaviour of a large marine four-stroke dual-fuel engine. Fuel. 281:118744. https://doi.org/10.1016/j.fuel.2020.118744
Watson N, Janota MS. 1982. Turbocharging the internal combustion engine. Macmillan Education UK.
Wei H et al. 2017. Effect of swirl flow on spray and combustion characteristics with heavy fuel oil under two-stroke marine engine relevant conditions. Appl Therm Eng. 124:302–314. https://doi.org/10.1016/j.applthermaleng.2017.05.202
Winterbone DE, Pearson RJ, Qatu M, Siavoshani S. 2001. Theory of engine manifold design: wave action methods for ic engineers. Appl Mech Rev. 54(6):B109–B110. https://doi.org/10.1115/1.1421124
Wurzenberger JC, Bartsch P, Katrasnik T. 2010. Crank-angle resolved real-time capable engine and vehicle simulation-fuel consumption and driving performance. SAE Technical Paper.
Xu S, Anderson D, Hoffman M, Prucka R, Filipi Z. 2017. A phenomenological combustion analysis of a dual-fuel natural-gas diesel engine. Proc Inst Mech Eng Pt D J Automobile Eng. 231(1):66–83.
Yeliana Y, Cooney C, Worm J, Michalek D, Naber J. 2011. Estimation of double-wiebe function parameters using least square method for burn durations of ethanol-gasoline blends in spark ignition engine over variable compression ratios and egr levels. Appl Therm Eng. 31(14-15):2213–2220. https://doi.org/10.1016/j.applthermaleng.2011.01.040
Zellbeck H, Kleinen M, Werner R. 2013. Neuer ansatz zur berechnung von radialverdichtern. MTZ-Motortech Z. 74(10):738–745. https://doi.org/10.1007/s35146-013-0223-2
Zhou X, Li T, Wei Y, Wu S. 2019. Scaling spray combustion processes in marine low-speed diesel engines. Fuel. 258:116133. https://doi.org/10.1016/j.fuel.2019.116133
Zinner K. 1975. Aufladung von verbrennungsmotoren. Springer.

Appendices

Appendix 1. Turbocharger design parameters

Table A1. Design parameters for compressor and turbine map prediction.

Machine Parameter	Value	Model Parameter	Value
Compressor prediction according to Casey and Robinson (2013)			
Impeller Tip Diameter D_2	0.094 02 m	Design Point Polytropic Efficiency η_{pol}	0.67
Impeller Outlet Width b_2	0.0175 m	Slip factor impeller outlet s	0.31
Impeller Blade Outlet Angle β_2	−25°	Disc friction coefficient k_{df}	0.002
Rotational Speed Design Condition n_0	60 100 rpm	Degree of Reaction Design Point γ_d	0.6
Massflow Design Condition $\dot{m}_0$	0.254 kg s^{-1}	Polytropic Exponent n_d	1.35
Pressure Ratio Design Condition π_0	1.502		
Inlet Pressure Design Condition $p_{in,0}$	100.3 kPa		
Inlet Temperature Design Condition $T_{in,0}$	311.35 K		
Compressor prediction according to Stapersma (2019)			
Efficiency Design Condition η_0	0.67	Sensitivity Parameter x	2
Rotational Speed Design Condition n_0	81 000 rpm	Sensitivity Parameter y	0.1
Massflow Design Condition $\dot{m}_0$	0.352 kg s^{-1}	Nominal Mach Number Ma_0	0.55
Pressure Ratio Design Condition π_0	1.845	Nominal Enthalpy Coefficient ψ_0	0.822
Inlet Pressure Design Condition $p_{in,0}$	100.1 kPa	Split Factor s	0.6
Inlet Temperature Design Condition $T_{in,0}$	310.35 K		
Turbine prediction according to Stapersma (2019)			
Efficiency Design Condition η_0	0.80	Sensitivity Parameter x	1.6
Rotational Speed Design Condition n_0	76 400 rpm	Sensitivity Parameter y	1
Massflow Design Condition $\dot{m}_0$	0.395 kg s^{-1}	Nominal Mach Number Ma_0	0.90
Pressure Ratio Design Condition π_0	0.545	Nominal Enthalpy Coefficient ψ_0	−3.5
Inlet Pressure Design Condition $p_{in,0}$	191.3 kPa	Split Factor s	0.0
Inlet Temperature Design Condition $T_{in,0}$	837.25 K		
Turbine prediction according to Jensen et al. (1991)			
Rotational Speed Design Condition n_0	84 000 rpm	Coefficient k_{11}	0.005
Massflow Design Condition $\dot{m}_0$	0.375 kg s^{-1}	Coefficient k_{12}	0.22
Pressure Ratio Design Condition π_0	0.5453	Coefficient k_{21}	0.045
Inlet Pressure Design Condition $p_{in,0}$	191.3 kPa	Coefficient k_{22}	1.11
Inlet Temperature Design Condition $T_{in,0}$	837.25 K		

Appendix 2. Remaining model parameters

Table A2. Remaining model parameters.

Feature	Value
Ambient Conditions	
Ambient Temperature T_{amb}	296.65 K
Ambient Pressure p_{amb}	102.9 kPa
Exhaust Back Pressure p_{exh}	107.8 kPa
Thermodynamic Properties	
Gas Constant Air R_a	287 J/kgK
Specific Heat at Constant Pressure of Air $c_{p,a}$	1004.5 J/kgK
Specific Heat at Constant Volume of Air $c_{v,a}$	717.5 J/kgK
Specific Heat Ratio of air κ_a	1.4
Density Air ρ_a	1.1455 kg m^{-3}
Gas Constant Exhaust Gas R_g	287 J/kgK
Specific Heat at Constant Pressure of Exhaust Gas $c_{p,g}$	1049 J/kgK
Specific Heat at Constant volume of Exhaust Gas $c_{v,g}$	762 J/kgK
Specific Heat Ratio of Exhaust Gas κ_g	1.38
Polytropic Exponent for Compression n_{com}	1.35
Polytropic Exponent for Expansion n_{exp}	1.38
Polytropic Exponent for the Blowdown Process n_{bld}	1.38
Fuel Properties	
Gas Constant Fuel R_{fuel}	518.28 J/kgK
Density Fuel ρ_{fuel}	0.8532 kg m^{-3}
Lower Heating Value h^L	32 360 kJ m^{-3}
Stoichiometric Air-to-Fuel Ratio σ	13.81

Appendix 3. Complete indexes of performance

		All			Steady State			Dynamic		
1CV-SimpleTC	Variable	MAE	MAPE	PPMCC	MAE	MAPE	PPMCC	MAE	MAPE	PPMCC
	'P_B [kW]'	5.24	2.25	0.99	1.09	0.67	1.00	18.20	7.20	0.96
	'n_eng [rpm]'	2.86	0.19	0.93	0.85	0.06	0.25	9.13	0.61	0.93
	'Thr_pos [%]'	3.94	12.30	0.94	3.32	6.48	0.97	5.87	30.47	0.90
	'n_TC [rpm]'		100.00			100.00			100.00	
	'p_ac [kPa]'	4.10	3.20	0.99	3.48	2.85	1.00	6.00	4.26	0.96
	'p_ir [kPa]'	6.13	5.54	1.00	5.68	5.19	1.00	7.55	6.61	0.98
	'p_er [kPa]'	3.14	2.17	0.99	2.35	1.68	1.00	5.61	3.70	0.97
	'eta_eng [%]'	0.92	3.19	0.89	0.53	2.04	1.00	2.14	6.79	0.63
	'dm_in [kg/s]'	0.03	5.58	0.97	0.02	3.25	1.00	0.06	12.88	0.87
	'dm_fuel [kg/s]'	0.00048	2.32	1.00	0.00037	1.88	1.00	0.00083	3.70	0.98

1CV-Caslen	Variable	MAE	MAPE	PPMCC	MAE	MAPE	PPMCC	MAE	MAPE	PPMCC
	'P_B [kW]'	4.80	2.05	0.99	1.09	0.64	1.00	16.35	6.40	0.96
	'n_eng [rpm]'	3.87	0.26	0.70	0.77	0.05	0.46	13.55	0.91	0.70
	'Thr_pos [%]'	4.07	12.03	0.93	3.30	6.28	0.97	6.51	30.05	0.87
	'n_TC [rpm]'	1927.54	4.20	0.99	1633.53	3.76	1.00	2844.37	5.54	0.97
	'p_ac [kPa]'	2.73	1.98	0.99	2.07	1.60	1.00	4.80	3.15	0.98
	'p_ir [kPa]'	6.17	5.50	0.99	5.69	5.20	1.00	7.67	6.42	0.98
	'p_er [kPa]'	3.08	2.09	0.99	2.35	1.67	1.00	5.37	3.39	0.97
	'eta_eng [%]'	0.90	3.09	0.89	0.53	2.04	1.00	2.03	6.35	0.61
	'dm_in [kg/s]'	0.03	5.54	0.97	0.02	3.24	1.00	0.06	12.72	0.86
	'dm_fuel [kg/s]'	0.00051	2.32	0.99	0.00035	1.72	1.00	0.00102	4.22	0.97

1CV-StaSta	Variable	MAE	MAPE	PPMCC	MAE	MAPE	PPMCC	MAE	MAPE	PPMCC
	'P_B [kW]'	3.96	1.77	0.99	1.11	0.66	1.00	12.87	5.25	0.98
	'n_eng [rpm]'	3.09	0.21	0.90	0.98	0.07	0.11	9.65	0.64	0.91
	'Thr_pos [%]'	2.98	10.91	0.94	2.24	4.49	0.98	5.29	30.96	0.91
	'n_TC [rpm]'	4802.13	10.33	0.99	4807.07	10.39	0.99	4786.15	10.12	0.97
	'p_ac [kPa]'	3.23	2.04	1.00	2.78	1.77	1.00	4.65	2.86	0.99
	'p_ir [kPa]'	6.18	5.53	1.00	5.70	5.21	1.00	7.67	6.52	0.98
	'p_er [kPa]'	2.60	1.81	1.00	2.36	1.68	1.00	3.35	2.20	0.99
	'eta_eng [%]'	0.90	3.10	0.90	0.54	2.06	1.00	2.03	6.37	0.64
	'dm_in [kg/s]'	0.03	5.21	0.98	0.02	3.23	1.00	0.05	11.41	0.90
	'dm_fuel [kg/s]'	0.00042	2.04	1.00	0.00035	1.73	1.00	0.00064	3.01	0.99

3CV-StaSta	Variable	MAE	MAPE	PPMCC	MAE	MAPE	PPMCC	MAE	MAPE	PPMCC
	'P_B [kW]'	4.93	2.11	0.99	1.12	0.64	1.00	16.84	6.70	0.97
	'n_eng [rpm]'	3.17	0.21	0.84	0.70	0.05	0.68	10.86	0.72	0.84
	'Thr_pos [%]'	2.62	10.29	0.91	1.75	3.67	0.97	5.34	30.96	0.84
	'n_TC [rpm]'	2946.41	5.59	0.99	2536.55	4.72	1.00	4231.27	8.34	0.96
	'p_ac [kPa]'	3.13	2.10	0.98	1.74	1.14	1.00	7.48	5.12	0.92
	'p_ir [kPa]'	2.59	2.61	0.99	1.62	1.79	1.00	5.64	5.16	0.97
	'p_er [kPa]'	3.59	2.53	0.99	3.03	2.18	1.00	5.34	3.61	0.97
	'eta_eng [%]'	0.77	2.67	0.90	0.37	1.47	1.00	2.02	6.41	0.66
	'dm_in [kg/s]'	0.02	4.76	0.98	0.01	2.64	1.00	0.05	11.40	0.90
	'dm_fuel [kg/s]'	0.00039	1.92	0.99	0.00025	1.35	1.00	0.00081	3.73	0.98

3CV-StaJen	Variable	MAE	MAPE	PPMCC	MAE	MAPE	PPMCC	MAE	MAPE	PPMCC
	'P_B [kW]'	4.16	1.79	0.99	1.11	0.67	1.00	13.69	5.29	0.97
	'n_eng [rpm]'	4.42	0.30	0.75	1.19	0.08	0.14	14.49	0.97	0.76
	'Thr_pos [%]'	3.73	10.96	0.94	2.98	5.71	0.97	6.05	27.37	0.89
	'n_TC [rpm]'	3993.92	7.19	0.99	3710.02	6.60	1.00	4889.08	9.07	0.98
	'p_ac [kPa]'	2.37	1.59	0.99	1.34	0.88	1.00	5.60	3.79	0.94
	'p_ir [kPa]'	4.56	4.09	1.00	4.15	3.83	1.00	5.86	4.90	0.98
	'p_er [kPa]'	5.84	4.37	0.99	5.48	4.24	1.00	6.96	4.79	0.97
	'eta_eng [%]'	0.75	2.56	0.89	0.38	1.48	1.00	1.91	5.93	0.61
	'dm_in [kg/s]'	0.02	4.92	0.97	0.01	2.67	1.00	0.06	11.95	0.87
	'dm_fuel [kg/s]'	0.00039	1.86	1.00	0.00025	1.36	1.00	0.00082	3.39	0.98

Appendix 4. Mean absolute percentage error (MAPE) comparison leave-One-Out

MAPE	Benchmark		without 20%		without 60%		without 80%		without 100%	
Variable	SS	Dyn	SS	Dyn	SS	Dyn	SS	Dyn	SS	Dyn
'P_B [kW]'	0.63	6.70	-0.07	0.15	0.00	-0.01	0.00	0.03	0.00	0.43
'n_eng [rpm]'	0.05	0.72	-0.01	0.01	0.00	0.00	0.00	0.01	0.00	0.14
'Thr_pos [%]'	4.89	30.96	-0.52	0.20	-0.12	-0.03	-0.33	-0.07	0.73	1.37
'n_TC [rpm]'	4.72	8.34	-0.05	-0.42	-0.32	-0.33	0.06	0.10	0.01	0.13
'p_ac [kPa]'	1.11	5.12	-0.21	-0.71	-0.27	-0.17	0.02	0.08	0.06	0.22
'p_ir [kPa]'	1.79	5.16	-2.67	-2.20	-0.02	0.04	-0.03	0.04	0.16	0.18
'p_er [kPa]'	2.17	3.61	0.54	0.21	0.06	0.07	-0.11	-0.02	0.17	0.17
'eta_eng [%]'	1.47	6.41	-2.02	0.07	-0.05	-0.03	-0.06	-0.04	0.01	0.22
'dm_in [kg/s]'	2.65	11.40	-1.64	-0.23	0.09	0.00	-0.22	-0.18	0.40	0.39
dm_fuel [kg/s]'	1.35	3.73	-2.16	-1.66	-0.04	0.00	0.01	0.09	0.08	0.35

Appendix 5. Time trace load step STANAG

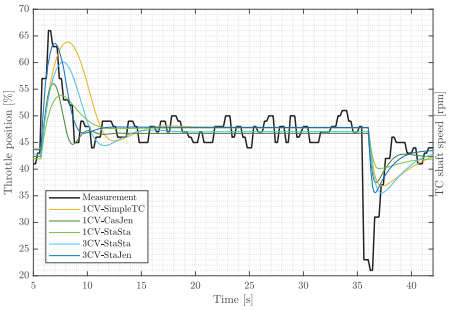

(a) Throttle Valve Position

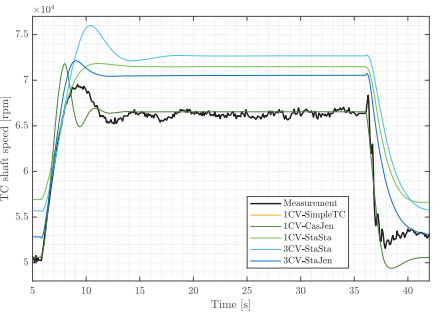

(b) Turbocharger Shaft Speed

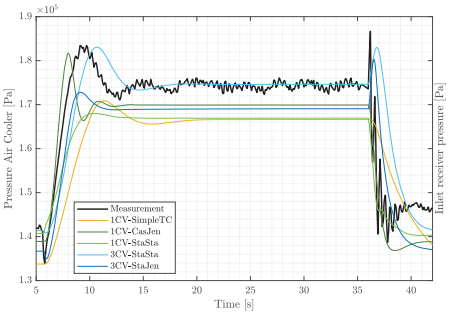

(c) Air Cooler Pressure

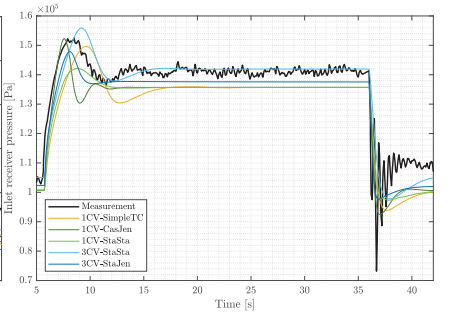

(d) Inlet Receiver Pressure

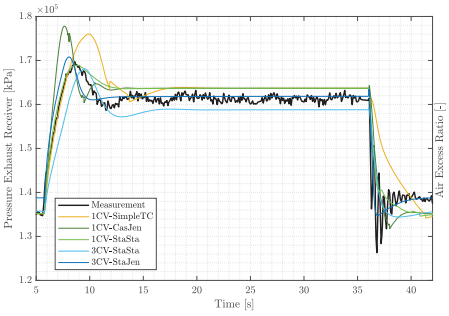

(e) Exhaust Receiver Pressure

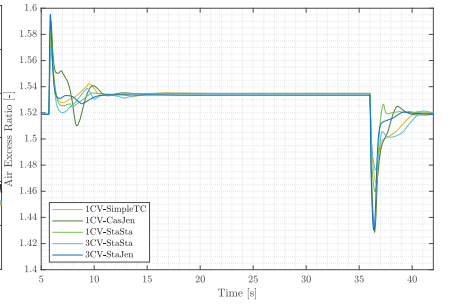

(f) Air-Excess Ratio

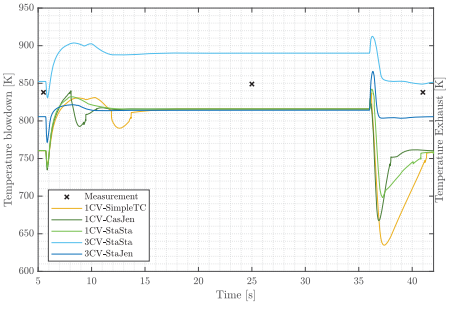

(g) Blowdown Temperature

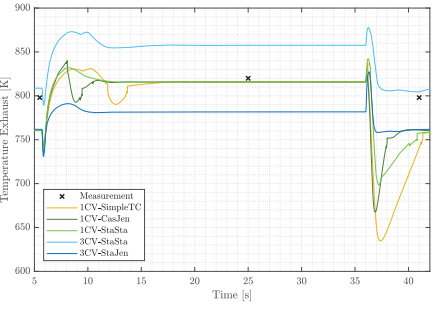

(h) Exhaust Receiver Temperature

Figure A19. Time trace plots of important dynamic engine parameters for a load increase from 200 kW to 305 kW and load decrease from 305 kW to 200 kW, complying with NATO STANAG 1008 for transient tolerance. (a) Throttle Valve Position. (b) Turbocharger Shaft Speed. (c) Air Cooler Pressure. (d) Inlet Receiver Pressure. (e) Exhaust Receiver Pressure. (f) Air-Excess Ratio. (g) Blowdown Temperature and (h) Exhaust Receiver Temperature.

Appendix 6. Time trace max load step

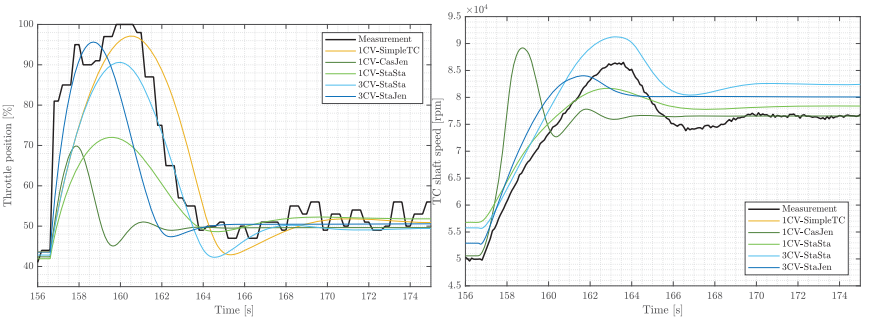

(a) Throttle Valve Position (b) Turbocharger Shaft Speed

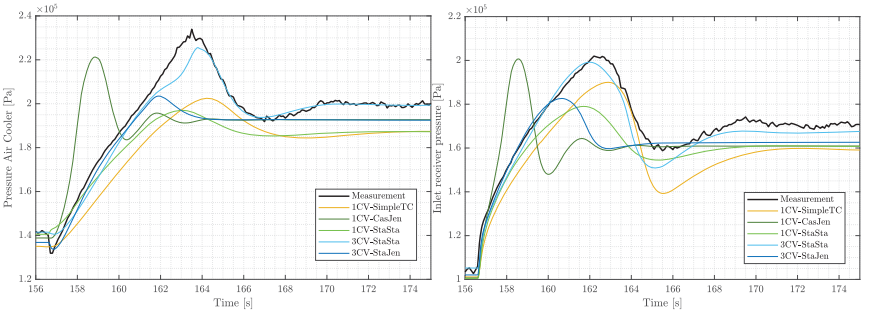

(c) Air Cooler Pressure (d) Inlet Receiver Pressure

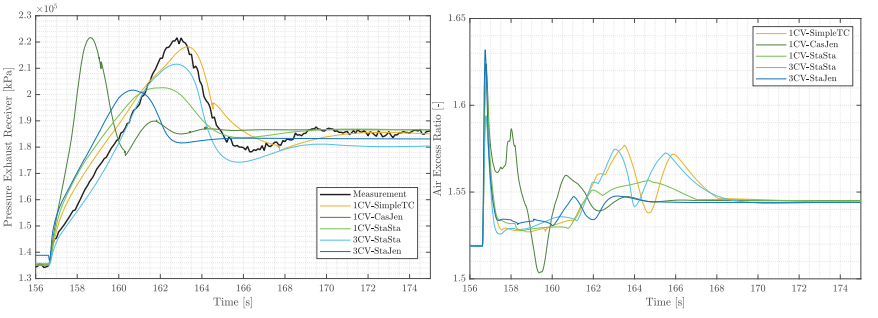

(e) Exhaust Receiver Pressure (f) Air-Excess Ratio

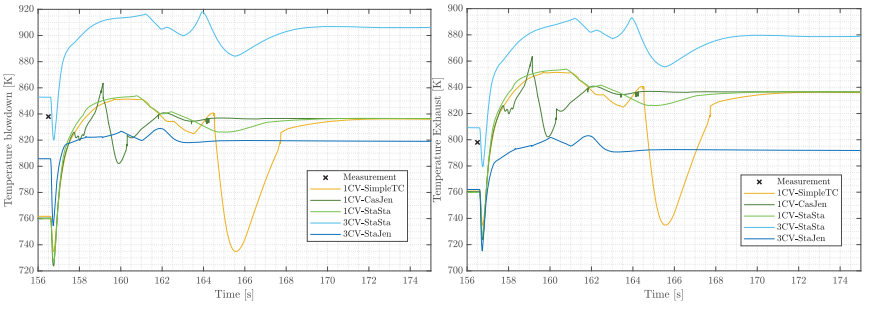

(g) Blowdown Temperature (h) Exhaust Receiver Temperature

Figure A20. Time trace plots of important dynamic engine parameters for a load increase from 200 kW to 380 kW. (a) Throttle Valve Position. (b) Turbocharger Shaft Speed. (c) Air Cooler Pressure. (d) Inlet Receiver Pressure. (e) Exhaust Receiver Pressure. (f) Air-Excess Ratio. (g) Blowdown Temperature and (h) Exhaust Receiver Temperature.